

H-shaped miktobrush copolymer nanoassembly facilitates ultrafast nucleus delivery for multi-stimuli-cooperative tumour suppression

Huabing Chen (✉ chenhb@suda.edu.cn)

Soochow University

Miya Zhang

Soochow University

Wenxue Dai

Soochow University

Tao Yang

Soochow University

Ting Li

Second Affiliated Hospital of Soochow University

Tao Xu

Second Affiliated Hospital of Soochow University

Yibing Deng

Jiangsu Key Laboratory of Translational Research and Therapy for Neuro-Psycho-Diseases

Hong Yang

Soochow University

Hengte Ke

Soochow University

Youliang Zhao

Soochow University

Article

Keywords: polymer nanoassembly, multi-stimuli responsiveness, nucleus delivery, triple negative breast cancer, photo-chemotherapy

Posted Date: February 4th, 2021

DOI: <https://doi.org/10.21203/rs.3.rs-155902/v1>

License:   This work is licensed under a Creative Commons Attribution 4.0 International License.

[Read Full License](#)

1 **H-shaped miktobrush copolymer nanoassembly facilitates**
2 **ultrafast nucleus delivery for multi-stimuli-cooperative**
3 **tumour suppression**

4 Miya Zhang^{1,2,#}, Wenxue Dai^{3,#}, Tao Yang^{1,2}, Ting Li^{1,2}, Tao Xu^{1,2}, Yibin Deng^{1,2}, Hong Yang¹,
5 Hengte Ke^{1,2,*}, Youliang Zhao^{3,*}, and Huabing Chen^{1,2,*}

6 ¹State Key Laboratory of Radiation Medicine and Protection, Soochow University, Suzhou 215123,
7 China

8 ²Jiangsu Key Laboratory of Neuropsychiatric Diseases, and College of Pharmaceutical Sciences,
9 Soochow University, Suzhou 215123, China

10 ³Suzhou Key Laboratory of Macromolecular Design and Precision Synthesis, Jiangsu Key
11 Laboratory of Advanced Functional Polymer Design and Application, State and Local Joint
12 Engineering Laboratory for Novel Functional Polymeric Materials, College of Chemistry,
13 Chemical Engineering and Materials Science, Soochow University, Suzhou 215123, China

14

15

16 Keywords: polymer nanoassembly, multi-stimuli responsiveness, nucleus delivery, triple-
17 negative breast cancer, photo-chemotherapy

18 #These authors contributed equally to this work.

19 *Correspondence and requests for materials should be addressed to H.C. (chenhb@suda.edu.cn),
20 Y.Z. (ylzhao@suda.edu.cn), H.K. (htke@suda.edu.cn).

21

22 **Abstract:** The potencies of antitumour compounds are often compromised by their restricted
23 subcellular delivery to nucleus, although a variety of smart vehicles have been extensively
24 designed to release drug in endocytic organelles. A major challenge remains in exploring the
25 nanocarriers with robust and spatiotemporal responsiveness for yielding efficient subcellular
26 targeting due to tumour heterogeneity. Herein, we show an H-shaped miktobrush copolymer
27 nanoassembly (NAs) with ultrafast nucleus delivery for multi-stimuli-cooperative suppression
28 against primary and metastatic triple-negative breast cancer (TNBC) models. The micellar NAs
29 display acidity- and glutathione-responsive drug releases through the protonation and disulfide-
30 bridge cleavage, which are further amplified by irreversible photo-controlled oxidation and phase
31 transition in a ratiometric manner, leading to rapid morphological destruction and ultrafast
32 cytoplasmic translocation into the nucleus from the lysosomes in a few minutes. These micellar
33 NAs thus show a distinctly enhanced cooperativity of photochemotherapeutic efficacy through
34 considerable apoptotic behavior, potently suppressing subcutaneous and orthotopic TNBC models,
35 together with enhanced survival rates. Moreover, these NAs yield preferable anti-metastatic
36 efficacy through the inhibition of metastasis-relevant proteins as compared to chemotherapy and
37 surgical resection. These results provide the insight into multi-stimuli-responsive polymers for
38 ultrafast nucleus delivery against aggressive tumours.

39

40 Triple-negative breast cancers (TNBC) have been widely considered as a highly aggressive
41 subtype with distinct risk of metastasis and recurrence that accounts for the leading mortality
42 among females. Versatile therapeutic approaches have been extensively explored to yield efficient
43 treatments against TNBC including chemotherapy, phototherapy, and immunotherapy, thereby
44 arousing great interests in developing high-performance vehicles such as micelles and vesicles that
45 combine two or more modalities to achieve considerable antitumour treatments against TNBC^{1,2}.
46 Reasonably, the precise delivery of vehicles incorporating antitumour cargoes to subcellular
47 targets is highly demanded to maximize antitumour efficacy with minimized adverse side effect
48 *via* enhanced tumour accumulation, deep penetration, intracellular drug release and accessibility
49 to subcellular target, reasonably leading to the widespread explorations of stimuli-responsive
50 nanoparticles for yielding potent antitumour efficacies³⁻⁷. For instance, various nanoparticles have
51 been rationally established to sense different endogenous stimuli such as mild acidity, enzyme,
52 glutathione and reactive oxygen species (ROS) that might promote intracellular drug release upon
53 endocytosis⁸⁻¹³. However, these stimuli-responsive nanoparticles frequently suffer from multiple
54 intracellular barriers including endocytic recycling routes that induces drug efflux, enzyme- or
55 acidity-mediated degradation, and restricted drug/nanoparticle diffusion into cytoplasm, thereby
56 compromising their ability to deliver cargoes to access ultimate subcellular targets such as nucleus
57 and mitochondria. Therefore, it is highly urgent to explore an efficient approach to deliver
58 therapeutic cargoes to precisely reach subcellular target for yielding potent therapeutics against
59 TNBC models, together with reduced tumour metastasis and recurrence.

60 Various smart designs of nanoparticle vehicles have been explored to maximize their drug
61 delivery efficiencies including multiple-stimuli combination, hierarchically multistage-stimuli
62 response, and spatiotemporal control *via* exogenous stimuli such as light, temperature and

63 ultrasound¹³⁻¹⁸, thus causing the interplay of a few responsive mechanisms such as hydrophobicity-
64 to-hydrophilicity conversion, charge conversion, chemical cleavage, and de-stabilization of weak
65 interactions (e.g. π - π stacking and hydrogen bonding) in the interior of vehicles for preferable drug
66 release and enhanced accessibility to cytoplasm. In particular, exogenous stimuli might offer
67 selective and on-demand release *via* precise manipulation on tumour site, while endogenous
68 stimuli are able to yield continuous drug release from the vehicles upon activation. However, the
69 expressions of endogenous stimuli molecules greatly vary in tumour cells including enzymes,
70 proteins, acidity and glutathione due to tumour heterogeneity, thus resulting in unsatisfied
71 exploration of robust and susceptible vehicles, and simultaneously the rational combination of
72 endogenous and exogenous stimuli also remains to be clarified for hurdling spatial barriers from
73 endocytic compartments to subcellular target¹⁴⁻²². Previously, we have explored light-responsive
74 nanoparticles that induce preferable drug release and efficient lysosomal rupture, thus promoting
75 considerable drug translocation into nucleus in ~ 30 min for enhanced antitumour efficacies against
76 TNBC^{14, 15, 23-30}. We hypothesize that the rational combination of multi-stimuli-responsive
77 interplay and light-induced lysosome-cytoplasm-nucleus pathway might promote rapid nucleus
78 delivery for yielding potent therapy against TNBC with favorable prognosis. Here, we report a
79 multi-stimuli-responsive H-shaped miktobrush copolymer nanoassembly incorporating
80 photochemotherapeutic cargoes with ultrafast nucleus delivery for potent suppression against
81 primary and metastatic TNBC (Fig. 1). The micellar nanoassemblies (NAs) that were constructed
82 using brush-like copolymer as the scaffold displayed the acidity- and glutathione-responsive drug
83 releases that were further amplified by both photo-oxidation and photo-hyperthermia in a
84 ratiometric manner, subsequently leading to ultrafast lysosome-to-cytoplasm-nucleus
85 translocation in 5 min (Fig. 1a and 1b). Then, the micellar NAs showed a distinctly enhanced

86 photochemotherapeutic efficacy through considerable apoptotic behavior, potently suppressing
87 subcutaneous and orthotopic TNBC models with enhanced survival rates, and simultaneously
88 generating considerable anti-metastatic efficacy as compared to chemotherapy and surgical
89 ablation through the inhibition of metastasis-relevant proteins.

90

91 **Results**

92 **Synthesis, preparation and characterization.**

93 To fabricate the multi-stimuli-responsive nanoassemblies, densely grafted brush-like copolymers
94 with two types of V-shaped heterografts were initially synthesized through a multi-step synthetic
95 route (Fig. 2a and Supplementary Fig. 1). The reductive-responsive disulfide group was introduced
96 from the initial chain transfer agent bis(2-hydroxyethyl)disulfide di(4-(benzodithioyl)-4-
97 cyanopentanoate) (S-CPDB), oxidative-responsive thioether groups were formed during thiol-
98 Michael addition reaction and thio-bromo click reaction, thermo-responsive poly(*N*-
99 isopropylacrylamide) (PNIPAM) was grown via thiolactone-based aminolysis and telomerization,
100 and pH-sensitive poly(acrylic acid) (PAA) was obtained by consecutive controlled radical
101 polymerization and hydrolysis. In addition, biodegradable poly(ϵ -caprolactone) (PCL) was grown
102 from the hydroxyl-bearing Y junctions connecting with PNIPAM or poly(*tert*-butyl acrylate)
103 (PtBA) to form V-shaped heterografts.

104 Firstly, the reversible addition-fragmentation chain transfer (RAFT) copolymerization of 4-
105 vinylbenzyl-3-(2-bromo-2-methylpropanoyloxy)-2-hydroxymethyl-2-methylpropionate (VBHP)
106 and 2-maleimidyl-4-thiobutyrolactone (MTL) afforded disulfide-linked poly(VBHP-*co*-MTL) (S1)
107 containing hydroxyl, alkyl bromide and thiolactone functionalities. The number of monomer units
108 given by ^1H NMR analysis was similar ($\text{DP}_{\text{VBHP}} \approx \text{DP}_{\text{MTL}} \approx 14$, Supplementary Fig. 2), which was

109 in good accordance with that expected from the alternating copolymerization system based on
110 styrene and maleimide. Secondly, disulfide-linked poly((St-*Pt*BA)-*co*-MTL) (S2) was synthesized
111 by combination of grafting-from strategy and end-capping reaction. The atom transfer radical
112 polymerization (ATRP) of *t*BA using S1 macroinitiator gave the desired graft copolymer with
113 DP_{PtBA} of 13.5, followed by the thio-bromo click reaction to de-activate terminal bromide
114 functionality (Supplementary Fig. 3). Thirdly, the tandem amine-thiol-telomerization reactions
115 using S2, ethanolamine, 2,2'-azobis(isobutyronitrile) and NIPAM as the raw materials were
116 adopted to generate disulfide-linked poly((St-*Pt*BA)-*co*-(MI-PNIPAM)) with DP_{PNIPAM} of 25 (S3,
117 Supplementary Fig. 4). Finally, the ring-opening polymerization of CL using S3 macroinitiator
118 afforded three examples of disulfide-linked poly((St-*Pt*BA/PCL)-*co*-(MI-PNIPAM/PCL))
119 copolymers (S4-S6), followed by selective hydrolysis using trifluoroacetic acid catalyst to
120 generate more hydrophilic disulfide-linked poly((St-PAA/PCL)-*co*-(MI-PNIPAM/PCL))
121 copolymers (H4-H6). In 1H NMR spectroscopy (Fig. 2b), the characteristic signals of various
122 segments were noted at 4.06 (CH_2O of PCL), 3.99 ($CHNH$ of PNIPAM), 2.31 (CH_2CO of PCL),
123 1.65 ($CH_2CH_2CH_2O$ of PCL), 1.44 (CH_3 of *Pt*BA), 1.38 ($CH_2CH_2CH_2O$ of PCL) and 1.14 ppm
124 (CH_3 of PNIPAM), and typical signals of CH_2 connecting with disulfide or thioether (CH_2S)
125 appeared at 2.5-3.1 ppm. After hydrolysis, the typical signal of *Pt*BA at 1.44 ppm disappeared
126 (Figure not shown). Based on 1H NMR analysis, the polymerization degree of PCL grafts was
127 about 11 (S4, H4), 18 (S5, H5) and 35 (S6, H6), respectively. The successful synthesis of the
128 desired heterografted copolymers and their precursors were confirmed by 1H NMR, GPC and FT-
129 IR spectra (Fig. 2b, Supplementary Fig. 2-6 and Table 1). The GPC traces of various copolymers
130 exhibited monomodal distribution (Supplementary Fig. 5). The apparent molar mass of S4-S6
131 ($M_{n,GPC} = 35.6-59.4$ kDa) was significantly lower than that given by 1H NMR analysis ($M_{n,NMR} =$

132 108-185 kDa), which could be ascribed to the reduced hydrodynamic volume of densely grafted
133 copolymers as compared to linear analogues originating from more compact structure.

134 The brush-like copolymer with reasonable lower critical transition temperature (LCST) of ~
135 39.4 °C (polymer H5, Fig. 2c) was mixed with indocyanine green (ICG) and doxorubicin (DOX)
136 in DMSO, and then the mixture was dispersed in water under ultrasonication, followed by the
137 formation of ICG/DOX-loaded micellar nanoassemblies (I/D-NAs) after the purification through
138 dialysis. The transmission electron microscopy (TEM) imaging shows that I/D-NAs with the
139 loading levels of 20% ICG and 10% DOX displayed the spherical morphology with the diameter
140 of 69.3 ± 5.6 nm (Fig. 3a). Dynamic light scattering (DLS) shows that the nanoassembly had an
141 average hydrodynamic diameter of 84.6 nm with polydispersity index of 0.173 (Supplementary
142 Fig. 7), and also exhibited a good size stability during 7 days (Supplementary Fig. 8).

143

144 **Photothermal and photodynamic properties.**

145 The UV-vis absorption of I/D-NAs was observed and the result displayed a broadened peak at 818
146 nm, which was red-shifted from the original peak of ICG at 778 nm (Fig. 3b), implying the
147 formation of the *J*-type and *H*-type ICG aggregates with intermolecular π - π stacking within the
148 nanoassemblies³¹⁻³³. I/D-NAs showed an enhanced photostability in aqueous solution, reasonably
149 due to the encapsulation and interaction of the encapsulated cargoes within the nanocarriers
150 (Supplementary Fig. 9). To characterize the photoconversion properties of the I/D-NAs, its
151 photothermal conversion behavior was evaluated under 785 nm light exposure. It showed their
152 photothermal conversion efficiency (η) of 24.6%, which was higher than that ($\eta = 20.3\%$) of free
153 ICG (Fig. 3c, Supplementary Fig. 10 and Table 2). Obviously, the nanoassembly displayed much
154 more temperature increase of 26.9 °C within 5 min at the dose of $10.0 \mu\text{g mL}^{-1}$ ICG as compared

155 to free ICG (~ 15.4 °C) and simultaneously exhibited a concentration-dependent improvement of
156 temperature (Supplementary Fig. 11). This result verifies that the I/D-NAs are able to maximize
157 the photothermal effect of photoactive agent that is highly favorable for hyperthermia-mediated
158 phototherapy, reasonably due to the enhanced non-radiative transition of encapsulated ICG
159 aggregates within the vehicles³¹⁻³³.

160 The electron spin resonance (ESR) was further used to monitor the singlet oxygen generation
161 from I/D-NAs using 2,2,6,6-tetramethylpiperide (TEMP) as the spin-trapping agent of singlet
162 oxygen³⁴. The nanoassemblies exhibited the characteristic 1:1:1 multiplicity of TEMP-1-oxyl
163 under 5 min light irradiation, confirming the singlet oxygen generation (Supplementary Fig. 12).
164 Afterwards, its singlet oxygen quantum yield (Φ_{Δ}) was further measured using 1,3-diphenyliso-
165 benzofuran (DPBF) as a reactive oxygen species (ROS) probe. Distinctly, I/D-NAs showed the
166 singlet oxygen quantum yield of 0.21, while free ICG only had the quantum yield of 0.14 (Fig. 3c
167 and Supplementary Table 3). Meanwhile, these nanoassemblies effectively yielded the singlet
168 oxygen in a time-dependent manner under light exposure, while distinctly reduced singlet oxygen
169 generation was observed for free ICG (Supplementary Fig. 13). Hence, these nanoassemblies also
170 afford considerable singlet-to-triplet transition and subsequent energy transfer to molecular
171 oxygen for more singlet oxygen generation in addition to photothermal effect, potentially
172 facilitating the lysosomal rupture in tumour cells.

173

174 **Multi-stimuli-responsive drug release.**

175 The multi-stimuli-responsive drug release behavior of I/D-NAs was evaluated in response to acidic
176 pH, reduction and NIR-light-triggered thermal and ROS stimuli (Fig. 3d). The results showed that
177 I/D-NAs alone at physiological pH 7.4 exhibited a relatively slow and insufficient release profile

178 of DOX compared to free ICG/DOX (Free I/D), confirming the reduced side effects from burst
179 release of chemotherapeutic drugs. Notably, I/D-NAs displayed the increased accumulative
180 releases of DOX at pH 5.0, and was further enhanced by the addition of 10.0 mM dithiothreitol
181 (DTT), reasonably being attributed to the deformation of PAA segments in acidic pH and disulfide
182 cleavage in reduction environment. Moreover, under light irradiation at 1.5 W cm⁻² for 5 min, the
183 accumulative release amount of DOX from I/D-NAs was significantly raised, reasonably due to
184 the deformation of PNIPAM and thioether segments caused by photo-hyperthermia and photo-
185 oxidation stimuli, as evidenced by the additionally increased DOX release by elevating the solution
186 temperature to 45 °C (higher than LCST of 39.4 °C). Interestingly, the light-enhanced responsive
187 release profile could be simply optimized through a ratiometric manner (Supplementary Fig. 14),
188 indicating that the ratio of 2:1 between encapsulated ICG and DOX might trigger greater
189 dissociation of micellar assemblies, thus favoring rapid lysosomal escape and cytoplasmic
190 translocation of antitumour drugs. Thus, I/D-NAs loading ICG/DOX at the ratio of 2:1 were
191 selected for their following *in vitro* and *in vivo* assessments. The multi-stimuli responsiveness of
192 I/D-NAs was further confirmed by the morphological changes upon various stimuli
193 (Supplementary Fig. 15). The TEM images displayed the obvious deformation of I/D-NAs upon
194 exposure to acidic or reduction conditions, and the morphological destruction was also observed
195 for I/D-NAs under light irradiation. It confirms the superiority of I/D-NAs as a smart vehicle for
196 cancer therapeutics.

197

198 **Cellular uptake and photo-induced lysosomal disruption.**

199 To investigate the endocytic capacity of I/D-NAs, the cellular uptakes of DOX were assessed after
200 6, 12, and 24 h incubation with 4T1 tumour cells. The internalized amounts of DOX in tumour

201 cells from I/D-NAs displayed the significantly improvement with time-dependency as compared
202 to Free I/D (Fig. 3e), indicating that these nanoassemblies possess a preferable capability to
203 improve the drug uptake. Subsequently, the cellular uptake pathway of I/D-NAs was demonstrated
204 in the presence of different endocytic inhibitors. I/D-NAs displayed a 28% decrease of DOX in
205 the cellular uptake upon treatment with chlorpromazine, indicating a clathrin-mediated energy-
206 dependent pathway of NAs (Fig. 3f). Afterward, the acridine orange (AO) staining was applied to
207 observe the destruction of lysosomes by ROS upon light irradiation. AO is an intracellular
208 indicator that emits red fluorescence in acidic lysosomes, and generates green fluorescence in
209 neutralized cytosol and nuclei. The lysosomes exhibited red fluorescence with PBS or irradiation
210 alone, indicating the intact lysosomes in the absence of I/D-NAs under irradiation or not. When
211 suffering from light irradiation, I/D-NAs at the dose of $2.0 \mu\text{g mL}^{-1}$ ICG resulted in obvious
212 lysosomal destruction, as evidenced by the disappearance of red fluorescence (Fig. 3g). In contrast,
213 free I/D at the same concentration still displayed the yellow fluorescence, thus confirming
214 preferable intracellular ROS generation from I/D-NAs upon light exposure (Fig. 3g). Obviously,
215 I/D-NAs can effectively destruct lysosomal membranes under light irradiation, effectively
216 facilitating the cytoplasmic release of DOX in tumour cells.

217

218 **Intracellular translocation from lysosomes to nucleus.**

219 The confocal laser scanning microscopy (CLSM) was used to demonstrate the intracellular
220 distribution of I/D-NAs and photo-induced cytoplasmic translocation of antitumour compounds
221 (Fig. 3h). I/D-NAs exhibited high co-localization of 92.0% in lysosomes without irradiation after
222 2 h incubation. However, after 5 min light irradiation at 1.5 W cm^{-2} , the DOX/lysosome co-
223 localization rate significantly decreased to 23.0%, and on the contrary, the red/blue co-localization

224 rate was increased to 35.0%, indicating that the light irradiation facilitates the fast lysosome-
225 cytoplasm-nucleus translocation of DOX at 5 min post-irradiation. Furthermore, the co-
226 localization rate of DOX with nucleus was increased to 85.0% after 15 min light exposure,
227 suggesting that the doxorubicin almost completely escaped from lysosomes to enter the nucleus
228 (Fig. 3i). The result shows that the rational combination of intrinsic acidic and reduced
229 environment in lysosomes, and NIR light-induced ROS and thermal stimuli, cooperatively
230 facilitates the deformation of I/D-NAs and lysosomal membrane rupture in a relatively short period
231 of time, resulting in considerable cytoplasmic translocation of DOX that further promotes the rapid
232 entry of DOX into the nucleus for subsequent DNA interaction to facilitate apoptosis^{23,35,36}.

233

234 **Synergistic cytotoxicity of photo-chemotherapy.**

235 The photo-chemotherapeutic synergistic cytotoxicity was explored against 4T1 murine TNBC
236 tumour cells with I/D-NAs or Free I/D for 24 h under light exposure or not (Fig. 4a and
237 Supplementary Fig. 16). I/D-NAs resulted in a concentration-dependent cytotoxicity with 4.3 μg
238 mL^{-1} $\text{IC}_{50(\text{ICG})}$ without irradiation, while Free I/D alone had relatively poor cytotoxicity (IC_{50} , 11.5
239 $\mu\text{g mL}^{-1}$ ICG), indicating the drug-loaded NAs could act as stimuli-responsive drug delivery
240 system to achieve enhanced chemotherapy *via* prominent cellular internalization and intrinsic
241 acidity- and reduction-responsive drug release. When exposed to 3 min light irradiation, I/D-NAs
242 showed an increased cytotoxicity with 2.2 $\mu\text{g mL}^{-1}$ $\text{IC}_{50(\text{ICG})}$, compared to Free I/D (IC_{50} 8.7 μg
243 mL^{-1} ICG), exhibiting a multi-stimuli-cooperative antitumour efficiency due to the synergistic
244 effect of light-induced photothermal/photodynamic cytotoxicity in addition to light-mediated
245 nucleus delivery of DOX. Moreover, the combination index (CI, $\text{CI} = D_A / \text{IC}_{50(A)} + D_B / \text{IC}_{50(B)}$), in
246 which D_A and D_B represent the concentrations of A and B at IC_{50} in the presence of both A and B;

247 $IC_{50(A)}$ and $IC_{50(B)}$ represent the values of IC_{50} in the presence of A or B only, respectively^{37, 38}) was
248 calculated to assess the synergistic effect between chemotherapy and phototherapy of I/D-NAs
249 under light irradiation. The ICG-loaded nanoassemblies (ICG-NAs) with light irradiation were
250 employed to determine the phototherapy effect of ICG alone, and their IC_{50} with light irradiation
251 was measured to be $9.4 \mu\text{g mL}^{-1}$ ICG. The CI values of I/D-NAs at various molar ratios of
252 ICG:DOX were also calculated (Fig. 4b and Supplementary Fig. 17), indicating that I/D-NAs with
253 molar ratios of 2:1 and 3:1 exhibited distinctive synergistic cytotoxicity ($CI < 0.8$) between
254 chemotherapy and phototherapy upon light irradiation, demonstrating a ratiometrically tunable
255 anticancer efficacy.

256

257 **Cell apoptosis.**

258 To investigate the cell damage mechanism of I/D-NAs, flow cytometry was utilized to detect
259 apoptotic levels using Annexin V-APC/DAPI staining. As shown in Fig. 4c and 4d, no obvious
260 apoptosis in tumour cells was observed for PBS with or without light irradiation, while Free I/D
261 exhibited 4.4% and 6.3% in early and late apoptosis under irradiation, respectively, indicating that
262 Free I/D can produce a mild apoptosis due to the combination of phototherapy and chemotherapy.
263 Whereas, the cells treated with ICG/DOX-loaded PEG-PCL micelles (I/D-Micelles) as a non-
264 responsive control exhibited a slight increased apoptotic effect at 15.3% and 12.7% for early and
265 late apoptosis in the absence of irradiation, respectively, and showed no significant increase of late
266 apoptosis upon light exposure. Importantly, I/D-NAs revealed a distinct improvement of apoptosis
267 in both early (44.9%) and late (25.4%) stage under irradiation *via* a prominent
268 photochemotherapeutic synergy, displaying a significant apoptotic increase as compared to I/D-
269 NAs without irradiation (22.7% and 15.3% in early and late apoptosis, respectively). Besides, ICG-

270 NAs as a control only facilitated the cell damage at 18.3% of early apoptosis and 7.6% of late
271 apoptosis. Hence, the potent apoptosis on tumour cells could be promoted through effective
272 synergistic photo-chemotherapy using multi-stimuli-responsive nanoassemblies.

273 In order to further assess the apoptotic mechanism of I/D-NAs, we examined the expression of
274 anti-apoptotic proteins and metastasis-relevant proteins in 4T1 cells with various treatments (Fig.
275 4e). The result displayed the lowest expressions of phosphorylated extracellular signal-regulated
276 kinase p-Erk1/2 (an anti-apoptotic protein that involves in tumour progression and metastasis in
277 the TNBC model³⁹) in tumour cells for I/D-NAs under light irradiation, while no obvious change
278 of p-Erk1/2 levels was found in other groups. Afterwards, the expression of Caspase-3 as a key
279 protein in execution-phase of cell apoptosis was then monitored, and the up-regulated expression
280 of Cl-Caspase-3 in 4T1 cells was observed for I/D-NAs under light irradiation, reasonably due to
281 their preferable photo-induced cytotoxicity as indicated in Fig. 4a. Furthermore, I/D-NAs also
282 resulted in the distinct decrease of *N*-Cadherin, a metastasis-relevant protein⁴⁰, indicating that
283 cooperative photochemotherapy is potentially capable of regulating anti-apoptotic and metastasis-
284 relevant proteins for the inhibition of tumour progression and metastasis.

285

286 **Pharmacokinetics and biodistribution.**

287 The blood circulation of I/D-NAs was determined through the pharmacokinetic assessment (Fig.
288 5a). I/D-NAs exhibited a DOX elimination half-life ($t_{1/2\beta}$) of 5.2 h, which is more than 4 times
289 longer when compared with that of Free I/D (1.2 h). Moreover, the $AUC_{0-\infty}$ value of I/D-NAs was
290 calculated to be 60.8, being a 3-fold increase as compared to Free I/D (Supplementary Table 3-4).
291 The targeting capability of I/D-NAs was further evaluated using *ex vivo* NIR fluorescent imaging
292 of the mice bearing 4T1 tumours. I/D-NAs displayed 4-fold increase of tumour accumulation of

293 ICG at 24 h post-injection as compared to Free I/D, due to the effective EPR effect of the micellar
294 NAs (Fig. 5b and 5c). Then, the biodistribution behavior of I/D-NAs was evaluated, and showed
295 their highest distribution ($\sim 3.8\%$ ID g^{-1}) of DOX in tumour at 24 hours after administration,
296 demonstrating their efficient targeting ability and reasonable time point for light irradiation (Fig.
297 5d and Supplementary Fig. 18). Distinctly, the preferable tumour accumulation and prolonged
298 circulation of I/D-NAs might facilitate prominent synergistic photo-chemotherapy against TNBC
299 tumours.

300

301 **Photo-induced hyperthermia and ROS.**

302 To investigate the *in vivo* photothermal effect of I/D-NAs at the tumour sites, the temperature
303 elevations in the tumour of the 4T1 tumour bearing mice under 5 min irradiation was recorded at
304 24 h post-injection. I/D-NAs raised the local temperature at tumour site by ~ 15 °C under
305 irradiation (1.5 W cm^{-2} , 7.5 mg kg^{-1} ICG) and showed a dose-dependent temperature elevation
306 behavior, being preferable to the mild hyperthermia ($\Delta T = 8$ °C) induced by Free I/D (Fig. 5e and
307 5f, Supplementary Fig. 19-21). Hence, I/D-NAs facilitate the direct damage against the tumour
308 through photo-induced hyperthermia (>45 °C), which might trigger the deformation of micellar
309 NAs to promote the release and delivery of DOX. To demonstrate the *in vivo* photodynamic effect
310 of I/D-NAs, we also detected the generation of ROS in tumour using dihydroethidium (DHE)
311 staining, which can produce red fluorescence by transforming into 2-hydroxyethidium. In Fig. 5f,
312 abundant ROS were generated from I/D-NAs in the tumour upon light irradiation, which were
313 more than 3-fold increase as compared to Free I/D (Supplementary Fig. 21). Thus, I/D-NAs
314 facilitate potent ROS generation for triggering oxidation-responsive release of DOX and
315 subsequent ultrafast lysosome-cytoplasm-nucleus delivery.

316

317 **Antitumour efficacy on TNBC tumours.**

318 To elucidate the synergistic tumour suppressive efficacy, I/D-NAs, Free I/D, I/D-Micelles and
319 ICG-NAs were intravenously into the subcutaneous 4T1 TNBC tumour models at the dose of 7.5
320 mg kg⁻¹ ICG under 3 min irradiation or not, respectively. Subsequently, the tumour volume and
321 the survival rate were monitored during 60 days post-irradiation (Fig. 5g and 5h). It shows that
322 PBS revealed the rapid tumour growth regardless of irradiation, suggesting that NIR light alone
323 have no impact on tumour growth. Free I/D and I/D-Micelles as the control exhibited a slight
324 tumour growth suppression and the survival time of mice was relatively short (less than 30 days)
325 as well, indicating that the synergistic photo-chemotherapeutic effect of ICG/DOX in a free form
326 and non-responsive micelles is not so potent to generate sufficient anticancer efficacy. ICG-NAs
327 with light exposure caused the tumour ablation for a short period of time, yet followed by the rapid
328 recurrence and regrowth of tumours. It shows that the phototherapy alone was not able to facilitate
329 sufficient and sustained tumour damage. Remarkably, I/D-NAs with light irradiation had the
330 prominent inhibition against tumour recurrence with prolonged survival time, revealing the
331 preferable antitumour efficacy achieved by potent synergistic photo-chemotherapy *via* the multi-
332 stimuli-responsive cooperativity of the nanoassemblies of rationally designed brush-like
333 copolymer. Taking advantage of intrinsic acidic and reduction environment in lysosomes, as well
334 as NIR light-induced ROS and thermal stimuli, the deformation of I/D-NAs and lysosomal
335 membrane rupture could be effectively utilized to undergo cytoplasmic translocation and ultrafast
336 nucleus delivery for causing prominent antitumour efficacy. Therefore, the light exposure of I/D-
337 NAs at tumour could not only trigger immediate and severe cell damage *via* photo-induced

338 hyperthermia and ROS damage, but also facilitate the rapid lysosome-cytoplasm-nucleus delivery
339 of DOX to maximize photochemotherapeutic damage.

340 The hematoxylin and eosin (H&E) staining suggests that I/D-NAs upon light irradiation resulted
341 in most severe cell injury with strong hemorrhagic inflammation at tumour due to the potent photo-
342 chemotherapy (Supplementary Fig. 22), while PBS as control showed no obvious tumour damage
343 regardless of light exposure. In addition, I/D-NAs had no remarkable damage on heart, liver,
344 spleen, lung and kidney of the tumour-bearing mice (Supplementary Fig. 23) with no significant
345 body weight loss (Supplementary Fig. 24), indicating that multi-stimuli-cooperative
346 nanoassemblies have a negligible side effect on the normal tissues, making them a promising
347 candidate for cancer therapy.

348

349 **Inhibition against primary TNBC tumour and metastatic nodules in lung.**

350 Inspired by the successful application of I/D-NAs against subcutaneous 4T1 models, we further
351 utilized I/D-NAs to treat highly aggressive orthotopic 4T1-Luc breast tumours that frequently
352 causes metastatic nodules in lungs. The tumour growth profile, bioluminescence images and
353 photos of harvested tumours were monitored during the experiment. PBS as a control exhibited
354 significant aggressive primary tumour growth regardless of irradiation or not (Fig. 6a-c). Free I/D
355 showed a slight inhibition of tumour growth even upon light irradiation, mainly due to rapid
356 elimination of free drugs in blood circulation. I/D-Micelles as non-responsive nanocarrier
357 exhibited the enhanced antitumour effects as compared to Free I/D, probably resulting from their
358 EPR effect. The surgery and ICG-NAs with irradiation were also found to cause temporary
359 ablation of tumours for a relative short period of time, but accompanied by obvious tumour
360 recurrence and regrowth at day 7 and day 13, respectively. Notably, total tumour ablation of the

361 orthotopic breast tumour could be achieved by I/D-NAs under light irradiation, together without
362 any recurrence (Supplementary Fig. 25). Moreover, the observations of primary tumours using
363 H&E staining, TUNEL, and Ki67 immunostaining showed that I/D-NAs with light exposure
364 caused the strongest destructive damage with less cell proliferation and more severe apoptotic level
365 (Supplementary Fig. 26), confirming their potent antitumour efficacy against primary tumours for
366 potentially preventing the survival and escape of tumour cells⁴¹.

367 Afterwards, the bioluminescence images of primary tumours, metastatic nodules in the lungs
368 and H&E staining of lung section from the mice bearing orthotopic 4T1 tumours were further
369 observed. It shows that there was no significant bioluminescence from primary tumours and almost
370 no metastatic tumour nodules in the lungs for the mice treated with I/D-NAs under light irradiation
371 (Fig. 6d and 6e), indicating their significant anti-metastasis capability upon light exposure as
372 compared to surgical resection and ICG-NAs. The preferable inhibition of I/D-NAs against tumour
373 metastasis was in accordance with their capability to down-regulate the metastasis-related proteins
374 as indicated in Fig. 4e. In addition, no significant body weight loss was detected in the mice treated
375 with I/D-NAs upon light irradiation (Supplementary Fig. 27). Thus, I/D-NAs facilitate potent
376 cooperative photo-chemotherapeutic efficacy against orthotopic TNBC tumours and metastatic
377 nodules in the lungs through multi-stimuli-responsive drug release and ultrafast nucleus delivery.

378

379 **Discussion**

380 Endogenous stimuli are widely applied to trigger responsive drug release of smart vehicles for
381 improved chemotherapy⁴²⁻⁴⁵, and endogenously stimuli-responsive vehicles usually need to spend
382 several hours to accomplish the lysosome-cytoplasm-nucleus pathway^{46, 47}. In our design of H-
383 shaped miktobrush copolymer, there is only one disulfide bridge in a single polymer, which might

384 consume less glutathione to be cleaved as compared to the conventional polymers with one
385 disulfide in each monomer, implying that the cleavage of H-shaped structure is robust in response
386 to glutathione. In particular, this copolymer containing PAA and PNIPAM chains as hydrophilic
387 segments not only affords a prolonged circulation ($t_{1/2\beta}$, 5.2 h) as compared to that of Free I/D ($t_{1/2\beta}$,
388 1.2 h), but also easily transits to be hydrophobic upon protonation and hyperthermia at tumour for
389 causing rapid phase transition of copolymer to release drug. However, the conventional
390 poly(ethylene glycol) (PEG) as an extensively used hydrophilic segment only provide a stealthy
391 function in blood, together without any other functionality for smart release. Moreover, the rational
392 combination of endogenous and exogenous stimuli not only amplified drug release of I/D-NAs,
393 but also effectively destructed spatial barriers in tumour cells such as the capture of endocytic
394 compartments and limited drug diffusion to subcellular target¹⁴⁻²². In our previous studies, light-
395 responsiveness facilitated efficient lysosomal rupture through photo-induced singlet oxygen and
396 hyperthermia, resulting in considerable drug delivery into nucleus in ~ 30 min for enhanced
397 antitumour efficacy^{14, 15, 23-30}. These rationally designed NAs possess the multi-stimuli-responsive
398 cooperativity (I/D-NAs) that results in the ultrafast lysosome-cytoplasm-nucleus translocation in
399 about ~ 5 min for potent therapy against primary TNBC tumours and lung metastasis. Reasonably,
400 this design of H-shaped miktobrush copolymer nanoassembly provides a sophisticated multiple
401 functionalization approach for efficient nucleus delivery of antitumour compounds.

402 In summary, the H-shaped miktobrush copolymer nanoassemblies were successfully
403 constructed, resulting in potent suppression against primary and metastatic TNBC through multi-
404 stimuli-cooperative photo-chemotherapy caused by the combination of considerable smart drug
405 release and ultrafast lysosome-cytoplasm-nucleus delivery. The micellar nanoassemblies
406 exhibited acidity- and glutathione-responsive drug release of photochemotherapeutic cargos at a

407 low consumption level of glutathione, which are further amplified by irreversible light-triggered
408 deformation in a ratiometric manner. These multi-stimuli-responsive design cooperatively leads to
409 the rapid phase transition from hydrophilic segments into hydrophobic chains and lysosomal
410 rupture, both of which account for the ultrafast delivery of cargo from the lysosomes into the
411 nucleus in ~ 5 min. The distinctly enhanced cooperativity of photochemotherapy was demonstrated
412 by considerable apoptotic behavior, potent suppression against tumour models, as well as
413 improved survival rates. Notably, these NAs also facilitated preferable anti-metastatic efficacy
414 through the inhibition of metastasis-relevant proteins as compared to chemotherapy and surgical
415 ablation. Our strategy provides a multi-stimuli-responsive nanoplatfom for ultrafast nucleus
416 delivery in cancer therapy.

417

418 **Methods**

419 **Preparation of I/D-NAs.** To prepare I/D-NAs, 2.0 mg ICG, 1.0 mg desalted DOX, and 10.0 mg
420 polymer H5 were mixed in 200 μ L of DMSO, and then the mixed solution was dispersed into 2.0
421 mL distilled water under ultrasonication (15 min). Subsequently, the solution of I/D-NAs were
422 obtained after purification *via* dialysis (cut-off 3.5 kDa MW, 24 h). All of the above procedures
423 were performed at 25 $^{\circ}$ C. According to similar procedures, PEG₄₅-*b*-PCL₆₀ diblock copolymer was
424 employed to prepare the micelles without any stimuli-responsiveness as the control nanoparticles
425 (I/D-Micelles). The free ICG/DOX samples (Free I/D) were prepared by dissolving the drugs in
426 5% DMSO aqueous solution.

427

428 **Characterization.** The morphology of I/D-NAs was observed using transmission electron
429 microscope (TEM, Tecnai-G20). The hydrodynamic diameters were measured using Zetasizer

430 ZS90 (Malvern, U.K.) at 25 °C. The drug loading and entrapment efficiency of ICG and DOX
431 within micelles were measured by using ultrafiltration centrifuge (Cut-off 10 KDa MW) at 4 °C.
432 The absorption spectra of ICG were measured using a UV-vis spectrophotometer (UV2600,
433 Shimadzu) and the fluorescent spectra of DOX were measured using Fluorescence
434 Spectrophotometer (LS 55, PerkinElmer).

435
436 **Drug release.** The drug release behaviors of DOX from I/D-NAs and Free I/D were evaluated by
437 the dialysis method. Samples (1.0 mL each) were added in various solutions including pH 7.4 and
438 pH 5.0 buffers in the presence of 10.0 mM DTT or not. Then, the solutions were performed in air
439 with a contrast temperature oscillator shaker at 37 °C. The concentration of ICG and DOX were
440 measured at 0.5, 1, 2, 4, 8, 12 and 24 h, respectively. For NIR-light-triggered drug release, the
441 amounts of DOX released from I/D-NAs were evaluated in pH 5.0 buffers in the presence of 10
442 mM DTT after 785 nm irradiation (1.5 W cm⁻², 3 min).

443
444 **Photothermal effect and photothermal conversion efficiency.** Free I/D and I/D-NAs (each 0.5
445 mL) at the concentration of 1.0, 2.0, 5.0, 10.0, 25.0 and 50.0 µg mL⁻¹ ICG were irradiated (785
446 nm, 1.5 W cm⁻²) for 300 s, and their temperature were monitored with a thermometer every 30 s.
447 To calculate the photothermal conversion efficiency, 0.5 mL of Free I/D and I/D-NAs of 10.0 µg
448 mL⁻¹ ICG were exposed to 785 nm laser at 1.5 W cm⁻² for 5 min, and then the laser were removed
449 to cool the solution down to room temperature, with the temperature of the solution recorded each
450 30 s. The photothermal conversion efficiency (η) is calculated by the following equation:

451

$$\eta = \frac{hA(T_{max} - T_{amb}) - Q_0}{I(1 - 10^{-A\lambda})}$$

452 where h is the heat transfer coefficient, A is the surface area of the container, T_{max} is the
453 maximum temperature during the process, T_{amb} is the surrounding ambient temperature, Q_0 is the
454 heat input rate due to light absorption of the solvent, I is the laser power, and A_λ is the absorbance
455 of the sample at an excitation wavelength of 785 nm.

456

457 **Quantum yield of singlet oxygen, ESR and fluorescence lifetime measurement.** To measure

458 the singlet oxygen quantum yield (Φ_A), I/D-NAs were evaluated with 1,3-diphenylbenzofuran

459 (DPBF) used as a probe, and indocyanine green (ICG) was used as a reference compound (Φ_A^{ICG}

460 = 0.14). The solutions of ICG and I/D-NAs containing DPBF (30.0 μ M) were irradiated by 785

461 nm laser at 1.5 W cm⁻² for 300 s, and the absorbance of DPBF at 417 nm were recorded. The

462 singlet oxygen quantum yield (Φ_A) of I/D-NAs were calculated using the following equation $\Phi_A =$

463 $\Phi_A^{ICG} \cdot W \cdot I^{ICG} / (W^{ICG} \cdot I)$, where W and W^{ICG} are the photobleaching rates of DPBF in the presence

464 of I/D-NAs and ICG, respectively; I and I^{ICG} are the rates of light absorption by I/D-NAs and ICG,

465 respectively. The electron spin resonance (ESR) technique was employed to distinguish the type

466 of ROS. ROS from I/D-NAs were monitored by mixing 5.0 μ L 2,2,6,6-tetramethylpiperide

467 (TEMP), which was used as the spin-trapping agent of singlet oxygen (¹O₂), with 100 μ L I/D-NAs,

468 followed by 785 nm irradiation at 1.5 W cm⁻² for 5 min. The ESR spectra of I/D-NAs in the

469 presence of TEMP without irradiation was collected as a control. For fluorescence lifetime

470 measurement, the UV absorption spectra of I/D-NAs and Free I/D were measured using a UV-Vis

471 spectrophotometer (UV2600, Shimadzu), and the fluorescence spectrum were recorded by a

472 fluorescence spectrophotometer (PerkinElmer LS 55). Then, the fluorescence quantum yields were

473 calculated by the following equation: $\Phi_{F(sample)} = (F_{sample}/F_{ref})(A_{ref}/A_{sample})(n_{sample}^2/n_{ref}^2)\Phi_{F(ref)}$, in

474 which F is the measured fluorescence (area under the emission peak), A is the absorbance at the

475 excitation position, n is the refractive index of the solvent. ICG in water was used as the reference
476 ($\Phi_{F(ref)} = 0.005$).

477
478 **Photostability and chemical stability.** To determine photostability, Free I/D and I/D-NAs (each
479 3.0 mL) at the concentration of $5.0 \mu\text{g mL}^{-1}$ ICG were irradiated (785 nm, 1.5 W cm^{-2}) for 0.5, 1,
480 2, 3, 5, 7 and 10 min, respectively, followed by the measurements of the absorbance of ICG using
481 a UV-vis spectrophotometer. To determine chemical stability, Free I/D and I/D-NAs (each 3.0 mL)
482 at the concentration of $10.0 \mu\text{g mL}^{-1}$ ICG were dispersed in various media including culture
483 medium, pH 7.4 buffer and pH 5.0 buffer, and then their absorbance and fluorescence spectra were
484 monitored at 0, 4, 8, 12, 24 and 48 h, respectively.

485
486 **Cellular uptake and endocytic pathways.** 4T1 tumour cells (1.0×10^6 /well) were seeded on six-
487 well culture plates and incubated overnight in 37°C with RPMI 1640 containing 10% FBS. Free
488 I/D and I/D-NAs were added into the wells for 6, 12 and 24 h incubation. ICG and DOX from the
489 cells were extracted using DMSO, and measured by UV-vis and fluorescent assay, respectively.
490 For endocytic pathway, PBS and different inhibitions ($10 \mu\text{g mL}^{-1}$ chlorpromazine, $100 \mu\text{g mL}^{-1}$
491 amiloride, $50 \mu\text{g mL}^{-1}$ nystatin) were added into the cells for 1 h incubation at 37°C or 4°C in
492 RPMI-1640 medium, respectively. Next, Free I/D and I/D-NAs at the concentration of $10.0 \mu\text{g}$
493 mL^{-1} ICG were added into the plate for 2 h incubation. Then the ICG and DOX amounts extracted
494 from the cells were analyzed using UV-vis and a fluorescence spectrophotometer.

495
496 ***In vitro* cytotoxicity and disruption of lysosomal membranes.** For *in vitro* cytotoxicity
497 assessment, 4T1 cells (5.0×10^3 /well) were treated with Free I/D and I/D-NAs at the various doses

498 of 0.4, 1.0, 2.0, 4.0, 8.0, 16.0 and 20.0 $\mu\text{g mL}^{-1}$ ICG for 24 h incubation, followed by 3 min
499 irradiation (785 nm, 1.5 W cm^{-2}) or not. Another 24 h later, the cell viability was evaluated using
500 MTT assay. To evaluate the disruption of lysosomal membranes, acridine orange (AO) was used
501 as an intracellular indicator of acidic lysosomes. The 4T1 cells (5.0×10^4 /well) were treated with
502 PBS, Free I/D and I/D-NAs at the dose of 2.0 $\mu\text{g mL}^{-1}$ ICG for 6 h at 37 °C. Then, the cells were
503 washed with PBS and incubated in fresh medium, followed by 3 min irradiation at 785 nm (1.5 W
504 cm^{-2}). After 1 h, the 4T1 cells were washed and incubated with AO (6.0 μM , 1.0 mL) for 30 min,
505 finally subjected to fluorescence microscopical observation.

506

507 **Intracellular distribution.** 4T1 cells (5.0×10^4 cells/well) in a glass bottom dish were treated with
508 I/D-NAs for 2 h at 37 °C, and then washed by PBS. For the sample without irradiation, 1.0 mL
509 Hoechst 33342 (1.0 $\mu\text{g mL}^{-1}$) was added and incubated for another 10 min at 37 °C. Then, 1.0 mL
510 LysoTracker Green DND-26 (100 nM) was added and incubated for another 5 min. For the sample
511 observed at 5 min post-irradiation, the cells were treated with 1.0 mL of Hoechst 33342 (1.0 μg
512 mL^{-1}) for 10 min at 37 °C, and then illuminated for 3 min at 785 nm (1.5 W cm^{-2}), followed by
513 incubation with 1.0 mL LysoTracker Green DND-26 (50 nM) for 5 min. For the sample observed
514 at 15 min post-irradiation, the cells were firstly illuminated, and then incubated with Hoechst
515 33342 and LysoTracker Green DND-26. Finally, the cells were observed using CLSM (Zeiss
516 LSM710).

517

518 **Apoptosis.** The mechanism of cell death was explored using Annexin V-APC Apoptosis Kit. The
519 4T1 cells (1.0×10^5 /well) were cultured in a 12-well plate and then treated with PBS, Free I/D,
520 I/D-Micelles, I/D-NAs, ICG-NAs at 20 $\mu\text{g mL}^{-1}$ ICG for 24 h incubation, followed by 3 min 785

521 nm irradiation at 1.5 W cm^{-2} or not. Another 6 h later, the cells were digested with trypsin without
522 EDTA and collected by centrifugation at 3000 rpm, and then washed twice using PBS. Afterwards,
523 the cells were stained with Annexin V-APC Apoptosis Kit and DAPI and further analysed by flow
524 cytometry (FC500, Beckman Coulter).

525

526 **Western blotting.** 4T1 cells (1.0×10^6 /well) were cultured in six-well plates and then incubated
527 with PBS, Free I/D, I/D-Micelles I/D-NAs and ICG-NAs for 24 h, followed by 3 min irradiation
528 (785 nm , 1.5 W cm^{-2}) or not. Another 6 h later, cells were washed twice by PBS and then lysed on
529 ice with lysate for 1 h. Subsequently, the proteins from the cells were extracted and the
530 concentrations of the proteins were measured by BCA protein assay (Thermo Fisher Scientific).
531 The proteins ($10.0 \mu\text{g}$) for each group were separated by a 10% SDS-polyacrylamide gel and then
532 transferred to a nitrocellulose membrane, blocked with 5% skim milk in TBST for 1 h. Then, the
533 membrane was incubated with anti-N-cadherin (CST), anti-Caspase-3 (CST), anti-CI-Caspase-3
534 (CST), anti-p-Erk (CST), anti-Erk (Santa Cruz Biotech) and GAPDH (Affinity) overnight at $4 \text{ }^\circ\text{C}$,
535 washed with TBST five times, followed by incubation with secondary antibody (ZSGB-BIO) for
536 1.5 h and visualized by an ECL-plus detection system (GE healthcare).

537

538 ***Ex vivo* NIRF imaging and biodistribution.** The female BALB/c mice bearing 4T1 tumour were
539 constructed by subcutaneously injecting 4T1 cells (2.0×10^6 cells/mouse) into the flanks. Then,
540 the mice were injected intravenously with Free I/D and I/D-NAs at the doses of 7.5 mg kg^{-1} ICG
541 ($n = 3$). Then, the various tissues including heart, liver, spleen, lung, kidney and tumour were
542 extracted from the mice at 6, 12, 24, 48 h post-injection. The *ex vivo* fluorescence imaging of
543 various tissues at 24 h post-injection was observed using IVIS Lumina II with the excitation

544 wavelength of 745 nm. For biodistribution, methanol was used to extract ICG and DOX from the
545 different tissues at various time. Finally, DOX and ICG amounts were determined using
546 fluorescence and UV spectrophotometer, respectively.

547
548 ***In vivo* thermography.** Free I/D and I/D-NAs were injected intravenously into the female BALB/c
549 mice bearing 4T1 tumours at the doses of 2.5, 5.0, and 7.5 mg kg⁻¹ ICG, respectively. Then, the
550 mice were irradiated for 3 min using a 785 nm laser (1.5 W cm⁻²) at 24 h post-injection, and an
551 infrared camera (FLIR E50) was used to monitor the temperature at the tumour region during the
552 irradiation.

553
554 ***In vivo* antitumour efficacy.** The female BALB/c mice bearing subcutaneous 4T1 tumours were
555 injected with PBS, Free I/D, I/D-Micelles, I/D-NAs and ICG-NAs at the dose of 7.5 mg kg⁻¹ ICG
556 on day 0, 2, and 4 *via* tail vein. At 24 h post-injection, the tumours of each group were irradiated
557 with 785 nm laser at 1.5 W cm⁻² for 3 min or not. The tumour growth was observed during the
558 following 30 days, then the volumes were measured using a vernier caliper and calculated by this
559 formula: $V = X \times Y^2 / 2$, in which X and Y represent the length and width of the tumour, respectively.
560 The survival rates of these mice were further observed during 60 days post-irradiation.

561
562 **Orthotopic triple-negative breast cancer (TNBC) model.** The female BALB/c mice bearing
563 orthotopic 4T1 breast tumours were made by injecting luc-4T1 cells into the fat pad of breast, and
564 then were injected with PBS, Free I/D, I/D-Micelles, I/D-NAs and ICG-NAs *via* the tail vein on
565 day 0, 2, and 4, followed with 3 min 785 nm irradiation at 1.5 W cm⁻² at the tumour site 24 h later.
566 For surgery group, the tumours were ablated on day 0. Then, the tumour volumes were measured

567 and calculated during the following 20 days. Moreover, the mice were injected with 200 μ L sodium
568 fluorescein solution at the concentration of 15.0 mg mL⁻¹ on day 0, 2, 6, 9, 12, 16, 20 and the
569 bioluminescence of mice was observed using IVIS Lumina II. On day 20, all the mice were
570 sacrificed to extract their tumours and lungs to image their *ex vivo* bioluminescence. In addition,
571 the tumours were weighted and the metastatic tumour nodules in the lungs were also counted.

572

573 **H&E, Ki67, and TUNEL staining.** The BALB/c mice bearing subcutaneous 4T1 tumours were
574 intravenously injected with PBS, Free I/D, I/D-Micelles, I/D-NAs and ICG-NAs at the dose of 7.5
575 mg kg⁻¹ ICG, followed with 3 min irradiation (785 nm, 1.5 W cm⁻²) or not at 24 h post-irradiation.
576 Another 6 h later, various tissues including heart, liver, spleen, lung, spleen and tumour were
577 extracted and stored in the 4% formaldehyde solution. Afterwards, each tissues was cut into thin
578 sections for H&E staining. The mice bearing orthotopic 4T1 tumours were treated with the same
579 procedure as described above, then the tumours were extracted and cut into slices for Ki67 and
580 TUNEL staining. Lungs extracted from TNBC models were further cut into slices for H&E
581 staining. Then, the sections for H&E and Ki67 staining were performed using IX73 bright field
582 microscope (Olympus), while the TUNEL-stained sections were observed using a confocal laser
583 scanning microscope (Zeiss LSM650).

584

585 **Statistical analysis.** All data were presented as the mean value \pm SD. Statistical analysis was
586 performed using two-tailed Student's *t* test or one-way ANOVA with Tukey's post hoc test.
587 Statistical significance was established at $p < 0.05$, where * $p < 0.05$, ** $p < 0.01$, and *** $p < 0.001$.

588

589 **Data availability.** The data that support the findings of this study are available within the paper
590 and its Supplementary Information files. Raw data are available from the corresponding authors
591 upon reasonable request.

592

593

594

595 **References**

- 596 1. van der Meel, R., *et al.* Smart cancer nanomedicine. *Nat. Nanotechnol.* **14**, 1007–1017
597 (2019).
- 598 2. Peer, D., *et al.* Nanocarriers as an emerging platform for cancer therapy. *Nat. Nanotechnol.*
599 **2**, 751–760 (2007).
- 600 3. Murakami, M., *et al.* Improving drug potency and efficacy by nanocarrier-mediated
601 subcellular targeting. *Sci. Transl. Med.* **3**, 64ra62 (2011).
- 602 4. Wang, A.Z., Langer, R. & Farokhzad, O.C. Nanoparticle delivery of cancer drugs. *Annu.*
603 *Rev. Med.* **63**, 185–198 (2012).
- 604 5. Shi, J., Kantoff, P.W., Wooster, R. & Farokhzad, O.C. Cancer nanomedicine: progress,
605 challenges and opportunities. *Nat. Rev. Cancer* **17**, 20–37 (2017).
- 606 6. Chen, G., Roy, I., Yang, C. & Prasad, P.N. Nanochemistry and nanomedicine for
607 nanoparticle-based diagnostics and therapy. *Chem. Rev.* **116**, 2826–2885 (2016).
- 608 7. Sun, Q., Zhou, Z., Qiu, N. & Shen, Y. Rational design of cancer nanomedicine:
609 nanoproperty integration and synchronization. *Adv. Mater.* **29**, 1606628 (2017).
- 610 8. Zhang, Z., *et al.* Near infrared laser-induced targeted cancer therapy using
611 thermoresponsive polymer encapsulated gold nanorods. *J. Am. Chem. Soc.* **136**,
612 7317–7326 (2014).
- 613 9. Chen, H., *et al.* Polyion complex vesicles for photoinduced intracellular delivery of
614 amphiphilic photosensitizer. *J. Am. Chem. Soc.* **136**, 157–163 (2014).
- 615 10. de la Rica, R., Aili, D. & Stevens, M.M. Enzyme-responsive nanoparticles for drug release
616 and diagnostics. *Adv. Drug Deliv. Rev.* **64**, 967–978 (2012).
- 617 11. Chen, H., *et al.* Precise nanomedicine for intelligent therapy of cancer. *Sci. China Chem.*
618 **61**, 1503–1552 (2018).
- 619 12. Ge, Z. & Liu, S. Functional block copolymer assemblies responsive to tumor and
620 intracellular microenvironments for site-specific drug delivery and enhanced imaging
621 performance. *Chem. Soc. Rev.* **42**, 7289–7325 (2013).
- 622 13. Guo, Z., *et al.* pH-sensitive polymeric micelles assembled by stereocomplexation between
623 PLLA-b-PLys and PDLA-b-mPEG for drug delivery. *J. Mater. Chem. B* **7**, 334–345 (2019).

- 624 14. Shanmugam, V., Selvakumar, S. & Yeh, C.S. Near-infrared light-responsive nanomaterials
625 in cancer therapeutics. *Chem. Soc. Rev.* **43**, 6254–6287 (2014).
- 626 15. Zhang, Z., Wang, J. & Chen, C. Near-infrared light-mediated nanoplatforms for cancer
627 thermo-chemotherapy and optical imaging. *Adv. Mater.* **25**, 3869–3880 (2013).
- 628 16. Yang, G., Liu, J., Wu, Y., Feng, L. & Liu, Z. Near-infrared-light responsive nanoscale drug
629 delivery systems for cancer treatment. *Coord. Chem. Rev.* **320-321**, 100–117 (2016).
- 630 17. Wang, J., *et al.* NIR-activated supersensitive drug release using nanoparticles with a flow
631 core. *Adv. Funct. Mater.* **26**, 7516–7525 (2016).
- 632 18. Cao, J., *et al.* Near-infrared light-triggered micelles for fast controlled drug release in deep
633 tissue. *Biomaterials* **34**, 6272–6283 (2013).
- 634 19. Luo, D., *et al.* Rapid light-triggered drug release in liposomes containing small amounts of
635 unsaturated and porphyrin–phospholipids. *Small* **12**, 3039–3047 (2016).
- 636 20. Luo, D., *et al.* Doxorubicin encapsulated in stealth liposomes conferred with light-triggered
637 drug release. *Biomaterials* **75**, 193–202 (2016).
- 638 21. Meng, Z., *et al.* NIR-laser-switched in vivo smart nanocapsules for synergic photothermal
639 and chemotherapy of tumors. *Adv. Mater.* **28**, 245–253 (2016).
- 640 22. Qian, C., *et al.* Light-activated hypoxia-responsive nanocarriers for enhanced anticancer
641 therapy. *Adv. Mater.* **28**, 3313–3320 (2016).
- 642 23. Wang, Y., *et al.* Light-responsive nanoparticles for highly efficient cytoplasmic delivery
643 of anticancer agents. *ACS Nano* **11**, 12134–12144 (2017).
- 644 24. An, X., *et al.* Rational Design of Multi-stimuli-responsive nanoparticles for precise cancer
645 therapy. *ACS Nano* **10**, 5947–5958 (2016).
- 646 25. Yang, X., *et al.* Near-infrared light-triggered, targeted drug delivery to cancer cells by
647 aptamer gated nanovehicles. *Adv. Mater.* **24**, 2890–2895 (2012).
- 648 26. Ma, Y., Huang, J., Song, S., Chen, H. & Zhang, Z. Cancer-targeted nanotheranostics:
649 recent advances and perspectives. *Small* **12**, 4936–4954 (2016).
- 650 27. Deng, Y., *et al.* Cyanine-anchored silica nanochannels for light-driven synergistic thermo-
651 chemotherapy. *Small* **13**, 1602747 (2017).
- 652 28. Yang, H., *et al.* Micelles assembled with carbocyanine dyes for theranostic near-infrared
653 fluorescent cancer imaging and photothermal therapy. *Biomaterials* **34**, 9124–9133 (2013).

- 654 29. Wan, Z., *et al.* Highly efficient hierarchical micelles integrating photothermal therapy and
655 singlet oxygen-synergized chemotherapy for cancer eradication. *Theranostics* **4**, 399–411
656 (2014).
- 657 30. Wang, Y., *et al.* Smart albumin-biomaterialized nanocomposites for multimodal imaging
658 and photothermal tumor ablation. *Adv. Mater.* **27**, 3874–3882 (2015).
- 659 31. Guo, Z., *et al.* Heavy-atom-modulated supramolecular assembly increases antitumor
660 potency against malignant breast tumors via tunable cooperativity. *Adv. Mater.* **n/a**,
661 2004225 (2020).
- 662 32. He, H., *et al.* Photoconversion-tunable fluorophore vesicles for wavelength-dependent
663 photoinduced cancer therapy. *Adv. Mater.* **29**, 1606690 (2017).
- 664 33. Ye, S., *et al.* Rational design of conjugated photosensitizers with controllable
665 photoconversion for dually cooperative phototherapy. *Adv. Mater.* **30**, 1801216 (2018).
- 666 34. Yang, T., *et al.* Bifunctional tellurium nanodots for photo-induced synergistic cancer
667 therapy. *ACS Nano* **11**, 10012–10024 (2017).
- 668 35. Wang, C., *et al.* Enhancing cell nucleus accumulation and DNA cleavage activity of anti-
669 cancer drug via graphene quantum dots. *Sci. Rep.* **3**, 2852 (2013).
- 670 36. Tian, W., Xie, X. & Cao, P. Magnoflorine improves sensitivity to doxorubicin (DOX) of
671 breast cancer cells via inducing apoptosis and autophagy through AKT/mTOR and p38
672 signaling pathways. *Biomed. Pharmacother.* **121**, 109139 (2020).
- 673 37. Chou, T. & Talalay, P. Analysis of combined drug effects: a new look at a very old problem.
674 *Trends Pharmacol. Sci.* **4**, 450–454 (1983).
- 675 38. Soriano, A.F., *et al.* Synergistic effects of new chemopreventive agents and conventional
676 cytotoxic agents against human lung cancer cell lines. *Cancer Res.* **59**, 6178 (1999).
- 677 39. Liu, W., *et al.* Clinical significance of pAkt and pErk1/2 expression in early-stage breast
678 cancer patients treated with anthracycline-based adjuvant chemotherapy. *Oncol. Lett.* **9**,
679 1707–1714 (2015).
- 680 40. Gayther, S.A., *et al.* Tagging single nucleotide polymorphisms in cell cycle control genes
681 and susceptibility to invasive epithelial ovarian cancer. *Cancer Res.* **67**, 3027 (2007).
- 682 41. Yu, G., *et al.* A discrete organoplatinum(II) metallacage as a multimodality theranostic
683 platform for cancer photochemotherapy. *Nat. Commun.* **9**, 4335 (2018).

- 684 42. Du, J., Lane, L.A. & Nie, S. Stimuli-responsive nanoparticles for targeting the tumor
685 microenvironment. *J. Control. Release* **219**, 205–214 (2015).
- 686 43. Li, R. & Xie, Y. Nanodrug delivery systems for targeting the endogenous tumor
687 microenvironment and simultaneously overcoming multidrug resistance properties. *J.*
688 *Control. Release* **251**, 49–67 (2017).
- 689 44. Li, Z., Song, N. & Yang, Y. Stimuli-responsive drug-delivery systems based on
690 supramolecular nanovalves. *Matter* **1**, 345–368 (2019).
- 691 45. Peng, M. Stimuli-responsive nanocarriers for drug delivery, tumor imaging, therapy and
692 theranostics. *Theranostics* **10**, 4557–4588 (2020).
- 693 46. Li, Q., *et al.* AIEgen-functionalized mesoporous silica gated by cyclodextrin-modified CuS
694 for cell imaging and chemo-photothermal cancer therapy. *ACS Appl. Mater. Interfaces* **10**,
695 12155–12163 (2018).
- 696 47. Xue, Y., *et al.* Enhanced targeted delivery of doxorubicin based on acid induced charge
697 reversal and combinational stimuli-responsive nanocarrier. *Adv. Eng. Mater.* **20**, 1701151
698 (2018).
- 699

700 **Acknowledgments**

701 M. Z. and W. D. contributed equally to this work. This work was supported by National Key R&D
702 Program of China (2020YFA0710700), National Natural Science Foundation of China (51873143,
703 21971181, 32071373, and 81871480), Key Research & Development Program of Jiangsu Province
704 (BE2020763) and Priority Academic Program Development of Jiangsu Higher Education
705 Institutions (PAPD). All animal experiment protocols were approved by the Animal Care and Use
706 Committee of Soochow University, and complied with all relevant ethical regulation.

707

708 **Author contributions**

709 H.C., Y.Z. and H.K. conceived the idea and supervised the project. M.Z., W.D., T.Y., and T.X.
710 performed the experiments. M.Z., W.D., H.K. and H.C. contributed to the scheme and figures.
711 H.K., Y.Z. and H.C. contributed to the revision of original draft. M.Z., T.L., Y.D., H.Y., Y.Z. and
712 H.C. performed the analysis of all the data. H.K., Y.Z. and H.C. prepared the manuscript. All the
713 authors discussed the results and commented on the manuscript.

714

715 **Competing interests**

716 The authors declare no competing financial interests.

717

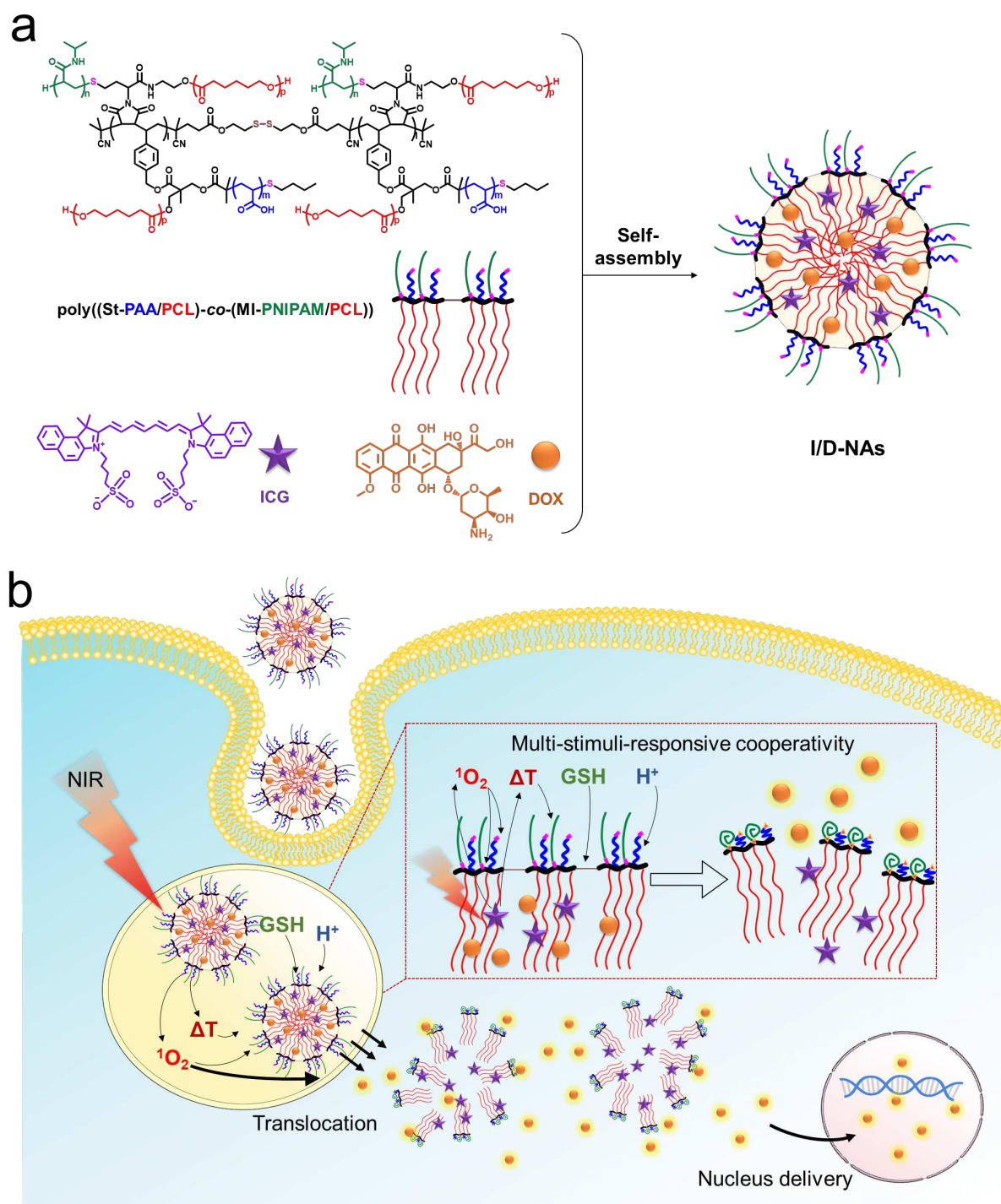
718 **Additional information**

719 Supplementary information is available for this paper.

720 Reprints and permissions information is available online at www.nature.com/reprints.

721 Correspondence and requests for materials should be addressed to H.C., Y.Z., H.K.

722



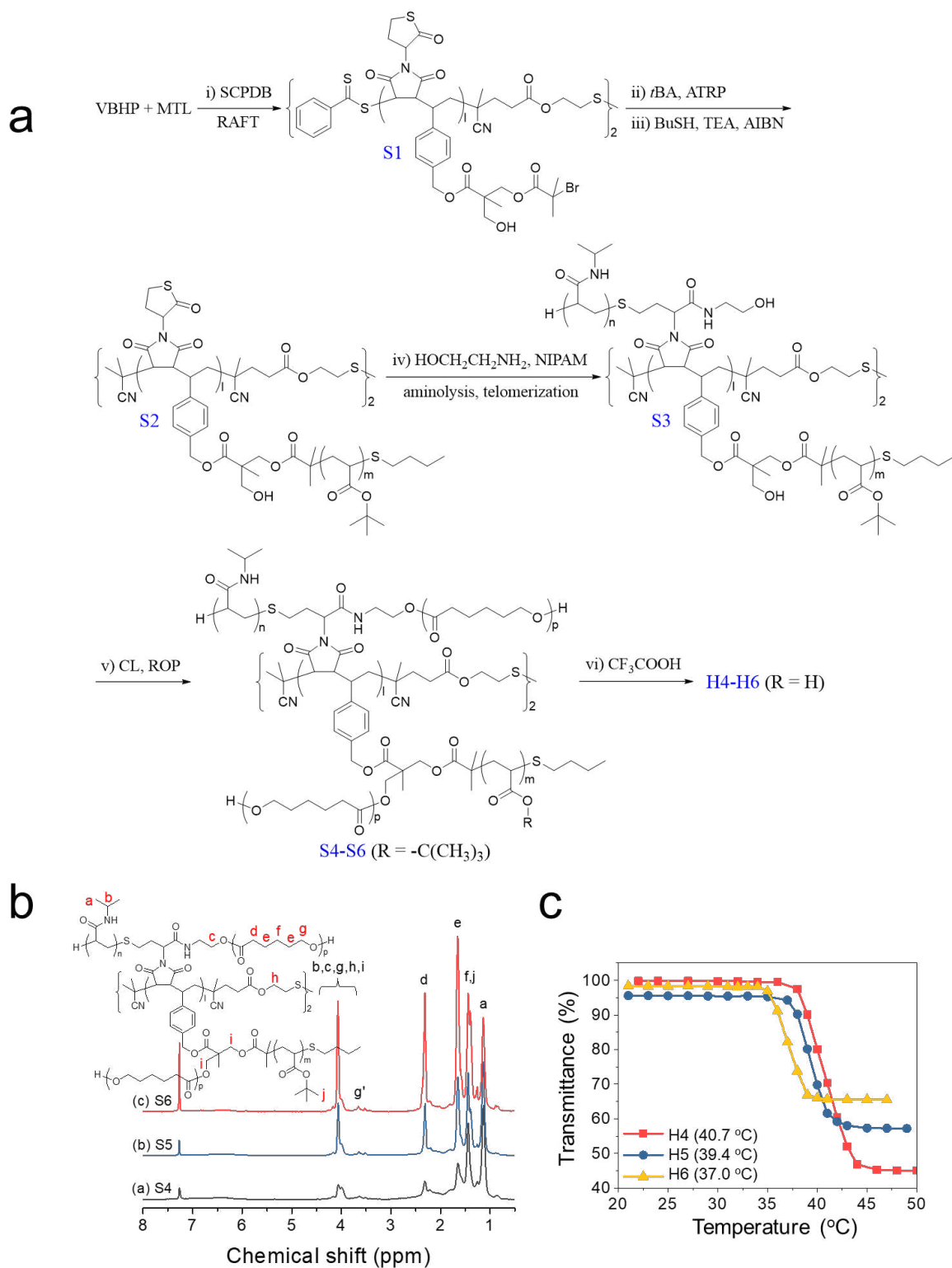
723

724 **Fig. 1. Schematic illustration of nanoassembly for anticancer therapy. a.** Construction of H-

725 shaped miktobrush copolymer nanoassemblies with pH/reduction/temperature/ROS-responsive

726 properties for co-encapsulating representative antitumour compounds such as indocyanine green

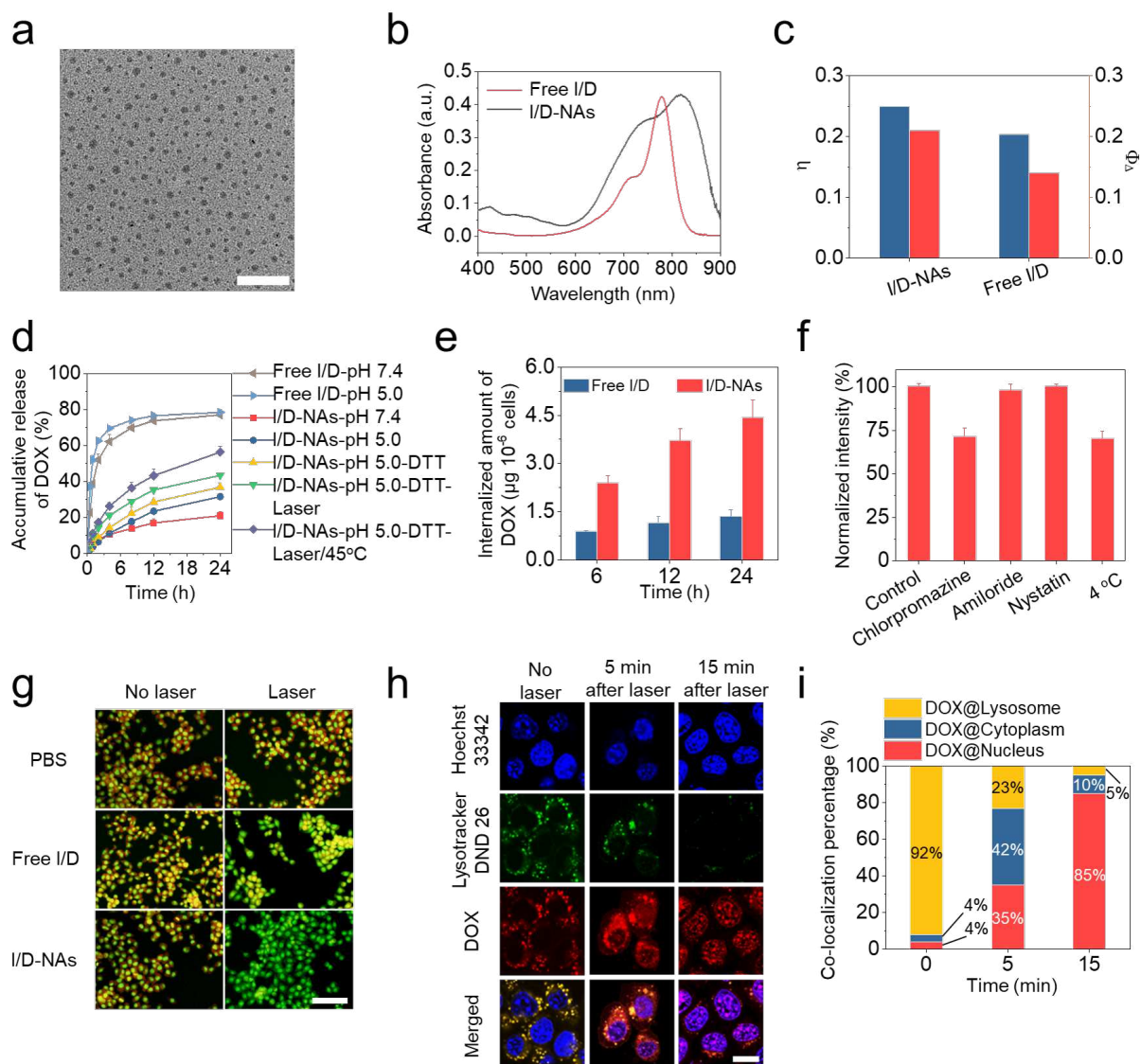
727 (ICG) and doxorubicin (DOX). **b.** Synergistic photo-chemotherapeutic mechanism against highly
728 aggressive TNBC tumours through multi-stimuli-responsive drug release and ultrafast nucleus
729 delivery.
730



731

732 **Fig. 2** Synthesis and characterization of brush-like copolymers. **a.** Synthesis of disulfide-
 733 bridged pH/reduction/temperature/ROS-responsive poly((St-*Pt*BA/PCL)-*co*-(MI-PNIPAM/PCL))

734 copolymers (H4-H6) by the combination of controlled polymerization, amine-thiol-telomerization
735 and selective hydrolysis, in which $l \approx 7$, $m \approx 14$, $n \approx 25$, and $p \approx 11$ (S4, H4), 18 (S5, H5) or
736 35 (S6, H6). **b.** ^1H NMR spectra of poly((St-*Pt*BA/PCL)-*co*-(MI-PNIPAM/PCL)) copolymers
737 recorded in CDCl_3 at 25 °C, where g' denotes terminal CH_2OH of PCL grafts. **c.** Influence of
738 temperature and chain length of PCL on transmittances of copolymer nanoassemblies ($c_p = 1.0 \text{ mg}$
739 mL^{-1}) formed from disulfide-bridged poly((St-PAA/PCL)-*co*-(MI-PNIPAM/PCL)) in aqueous
740 solution.
741



742

743 **Fig. 3. Enhanced lysosome-cytoplasm translocation and rapid nucleus delivery of I/D-NAs**

744 **by multi-stimuli-responsive cooperativity. a.** TEM image of I/D-NAs (scale bar: 500 nm). **b.**

745 UV-vis absorption of Free I/D and I/D-NAs. **c.** Photothermal conversion efficiency (η) and Singlet

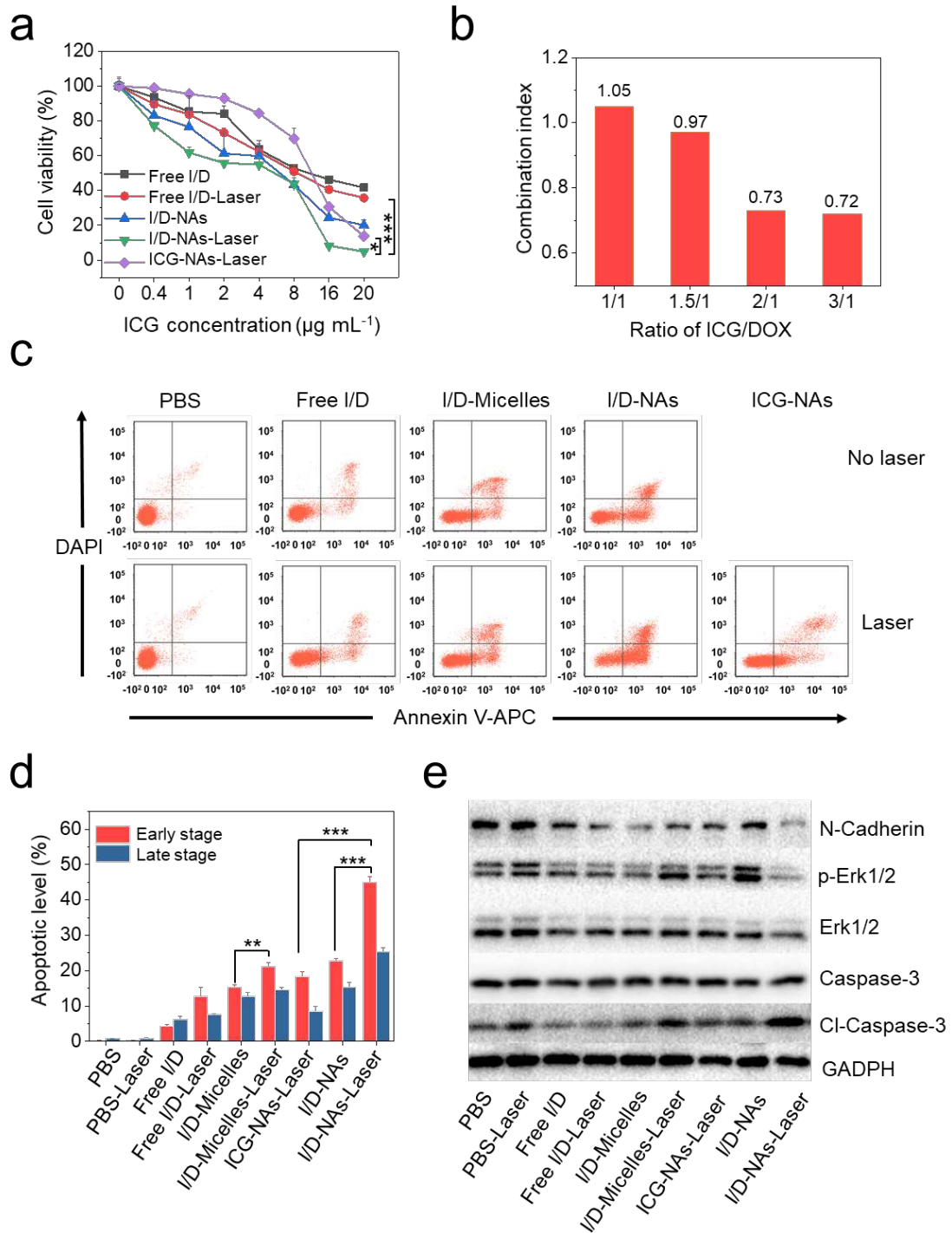
746 oxygen quantum yield (Φ_{Δ}) of Free I/D and I/D-NAs under 785 nm laser irradiation. **d.**

747 Accumulative releases of DOX from Free I/D and I/D-NAs in various solutions. **e.** Internalized

748 amounts of DOX in 4T1 cells treated by Free I/D and I/D-NAs at the dose of $10.0 \mu\text{g mL}^{-1}$ ICG

749 after 6, 12 and 24 h incubation. **f.** Cellular uptake by 4T1 cells treated with various inhibitors. **g.**

750 Lysosomal disruption of 4T1 cells treated with Free I/D and I/D-NAs under irradiation or not
751 (scale bar: 20 μm). **h.** Confocal laser scanning microscopy images (scale bar: 20 μm) of 4T1 cells
752 stained with LysoTracker Green DND-26 and Hoechst 33342 after 2 h incubation with I/D-NAs at
753 the dose of 10.0 $\mu\text{g ml}^{-1}$ ICG before irradiation, as well as 5 and 15 min post-irradiation (3 min,
754 1.5 W cm^{-2}), respectively. **i.** Co-localization percentage of DOX within different organelles as
755 indicated in **h.**
756



757

758 **Fig. 4. Cooperative cytotoxicity, antitumour and antimetastatic mechanisms of I/D-NAs. a.**

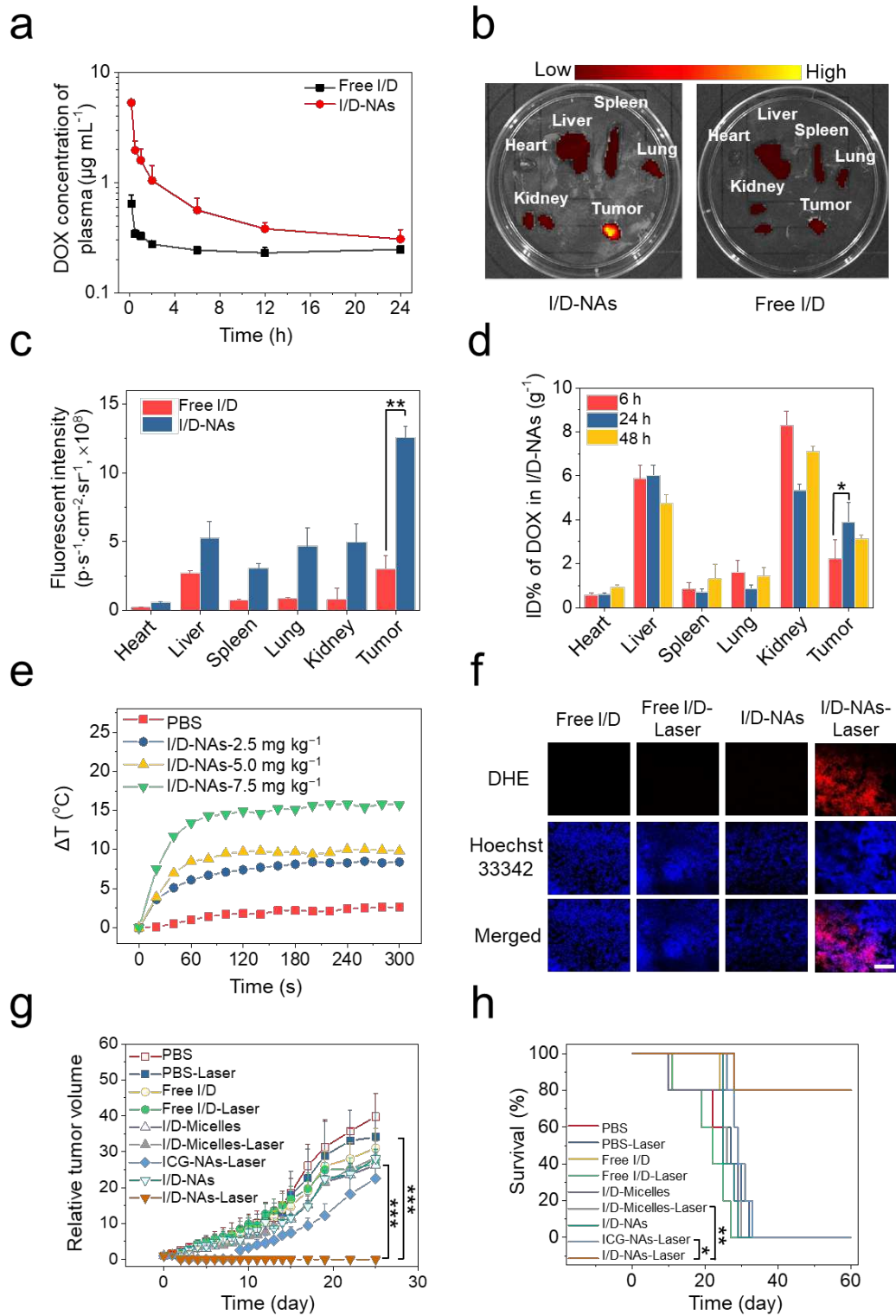
759 Cell viability of 4T1 cells treated with I/D-NAs and Free I/D under 1.5 W cm⁻² irradiation (785

760 nm, 3 min) or not. **b.** Combination index of I/D-NAs at various ratios of ICG:DOX. **c.** Apoptotic

761 levels of 4T1 cells stained by Annexin V-APC/DAPI Apoptosis Detection Kit after 24 h incubation
762 with PBS, Free I/D, I/D-Micelles and I/D-NAs at the dose of $10.0 \mu\text{g mL}^{-1}$ ICG under 3 min
763 irradiation (785 nm , 1.5 W cm^{-2}) or not and **(d)** their apoptotic percentages of early stage and late
764 stage. **e.** Western blotting of HSP 70, N-cad, p-ERK and Cl-caspase-3 levels at 6 h post-irradiation
765 in 4T1 cells after incubation with PBS, Free I/D, I/D-Micelles and I/D-NAs at the dose of $10.0 \mu\text{g}$
766 mL^{-1} ICG under 3 min irradiation (785 nm , 1.5 W cm^{-2}) or not. Statistical analysis was performed
767 using two-sided student's *t*-test, $*p < 0.05$, $**p < 0.01$, and $***p < 0.001$.

768

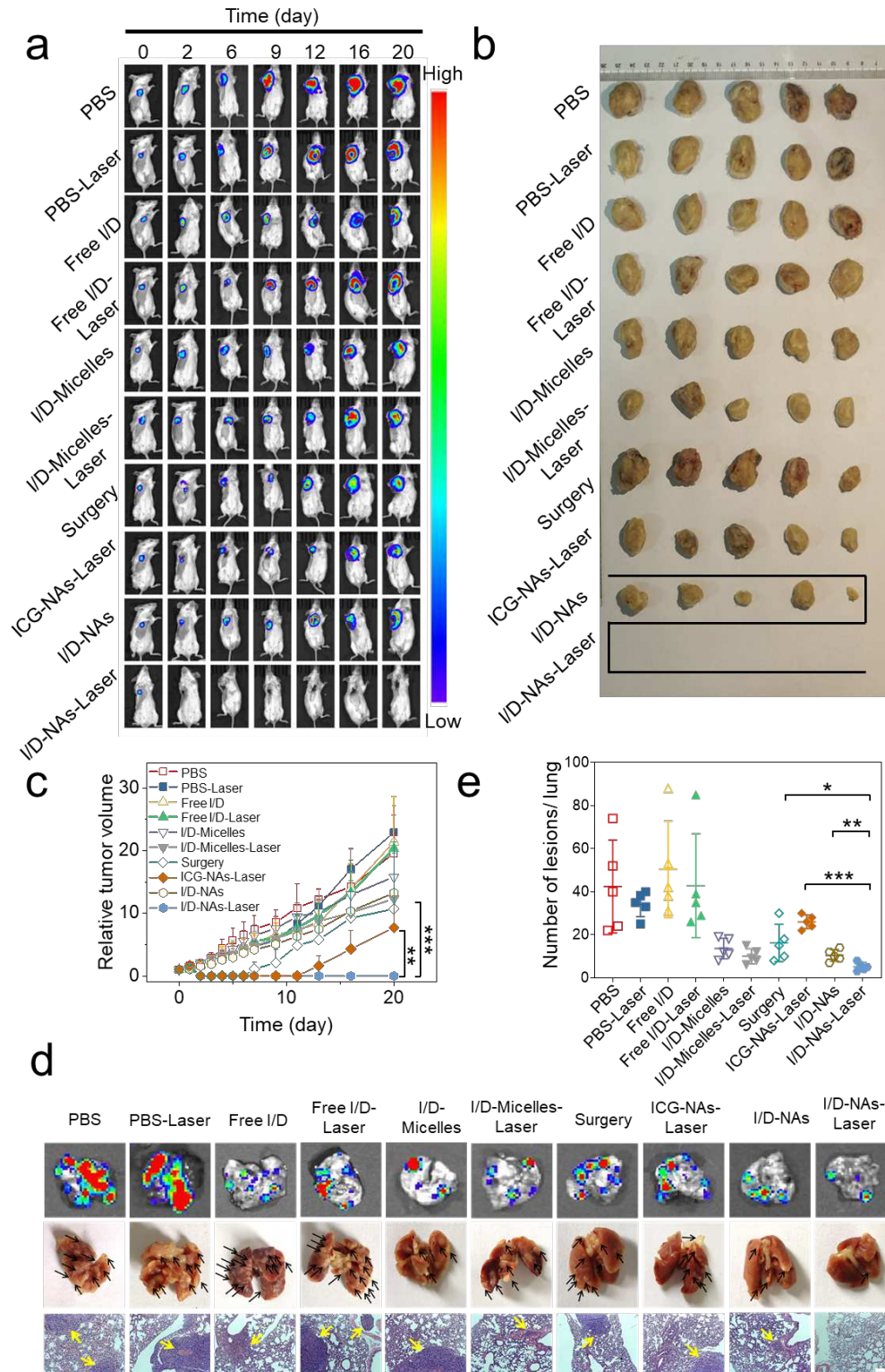
769



771

772 **Fig. 5. Photochemotherapeutic synergy of I/D-NAs against subcutaneous TNBC tumour**773 **models caused by multi-stimuli responsiveness. a. DOX concentrations in plasma from Free I/D**

774 and I/D-NAs at the dose of 7.5 mg kg⁻¹ ICG. **b.** *Ex vivo* NIRF images of heart, liver, spleen, lung,
775 kidney, and tumour extracted from the mice bearing 4T1 cells treated with Free I/D and I/D-NAs
776 at the dose of 7.5 mg kg⁻¹ ICG and **(c)** their NIRF intensities. **d.** Biodistribution of DOX in heart,
777 liver, spleen, lung, kidney, and tumour of the mice bearing 4T1 subcutaneous tumours treated with
778 I/D-NAs at different time post-injection at the dose of 7.5 mg kg⁻¹ ICG. **e.** Temperature elevations
779 of the mice bearing 4T1 cells treated with I/D-NAs at different doses of ICG under 785 nm
780 irradiation at 1.5 W cm⁻². **f.** DHE staining of tumour sections treated with Free I/D and I/D-NAs
781 at the dose of 7.5 mg kg⁻¹ ICG under 3 min irradiation or not (scale bar: 100 μm). **g.** Tumour
782 growth profiles of the mice bearing 4T1 subcutaneous tumours with various treatments at the dose
783 of 7.5 mg kg⁻¹ ICG, and **(h)** their Kaplan-Meier survival plots of the mice. The statistical analysis
784 was determined by two-sided student's *t*-test, ***p* < 0.01 and ****p* < 0.001. The statistical analysis
785 was carried out using two-sided log-rank (Mantel-Cox) test for **h**, **p* < 0.05 and ***p* < 0.01.
786



787

788 **Fig. 6. Photochemotherapeutic synergy of I/D-NAs against orthotopic and metastatic TNBC**

789 **tumour models. a.** *In vivo* bioluminescence images to track the tumour growth of the mice bearing

790 orthotopic 4T1 breast tumours after various treatments. **b.** The photographs of tumours extracted
791 from the mice at 20 days post-injection as indicated in **a.** **c.** Tumour growth profiles of mice with
792 various treatments as indicated in **a.** **d.** *Exo vivo* bioluminescence images, optical photographs and
793 H&E staining images (scale bar: 200 μm) of the lungs from the mice at 20 days post-injection as
794 indicated in **a.** **e.** Counts of metastatic nodules in the lungs of the mice at 20 days post-injection as
795 indicated in **a.** Statistical analysis was determined by two-sided student's *t*-test, * $p < 0.05$, ** $p <$
796 0.01 and *** $p < 0.001$.
797

798

Supplementary Information

799

800 **H-shaped miktobrush copolymer nanoassembly facilitates** 801 **ultrafast nucleus delivery for multi-stimuli-cooperative** 802 **tumour suppression**

803 Miya Zhang^{1,2,#}, Wenxue Dai^{3,#}, Tao Yang^{1,2}, Ting Li^{1,2}, Tao Xu^{1,2}, Yibin Deng^{1,2}, Hong Yang¹,
804 Hengte Ke^{1,2,*}, Youliang Zhao^{3,*}, and Huabing Chen^{1,2,*}

805 ¹State Key Laboratory of Radiation Medicine and Protection, Soochow University, Suzhou 215123,
806 China

807 ²Jiangsu Key Laboratory of Neuropsychiatric Diseases, and College of Pharmaceutical Sciences,
808 Soochow University, Suzhou 215123, China

809 ³Suzhou Key Laboratory of Macromolecular Design and Precision Synthesis, Jiangsu Key
810 Laboratory of Advanced Functional Polymer Design and Application, State and Local Joint
811 Engineering Laboratory for Novel Functional Polymeric Materials, College of Chemistry,
812 Chemical Engineering and Materials Science, Soochow University, Suzhou 215123, China

813

814

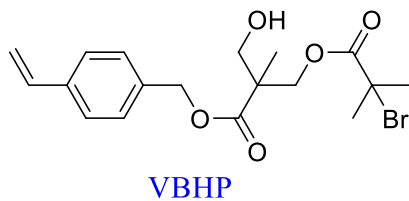
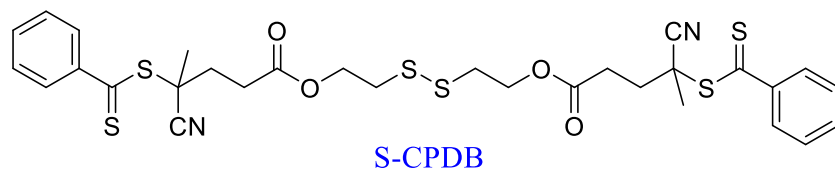
815 Keywords: polymer nanoassembly, multi-stimuli responsiveness, nucleus delivery, triple-
816 negative breast cancer, photo-chemotherapy

817 [#]These authors contributed equally to this work.

818 ^{*}Correspondence and requests for materials should be addressed to H.C. (chenhb@suda.edu.cn),
819 Y.Z. (ylzhao@suda.edu.cn), H.K. (htke@suda.edu.cn).

820

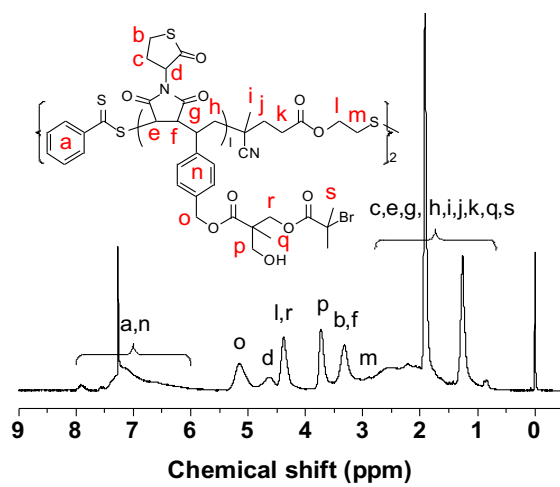
821 1. Supplementary Figures and Tables



822

823 **Supplementary Fig. 1.** Chemical structures of functional reagents S-CPDB, VBHP and MTL.

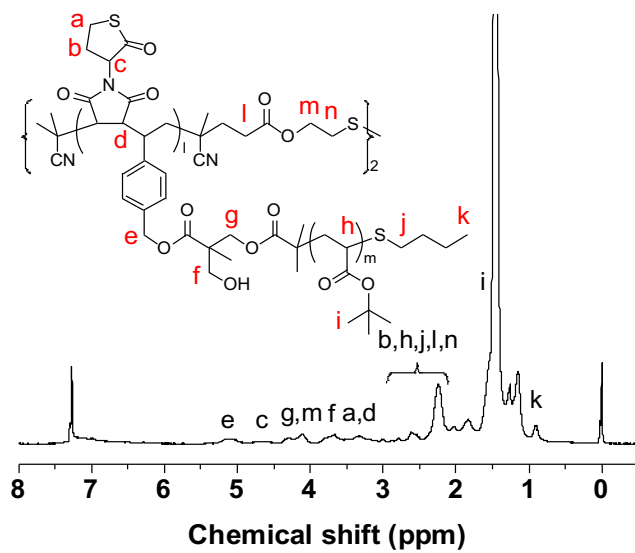
824



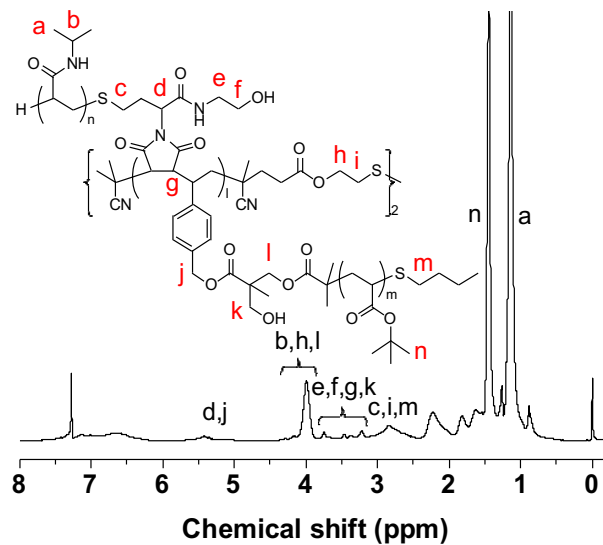
825

826 **Supplementary Fig. 2.** ¹H NMR spectrum of P(MTL-co-VBP) (S1) recorded in CDCl₃ at 25 °C.

827



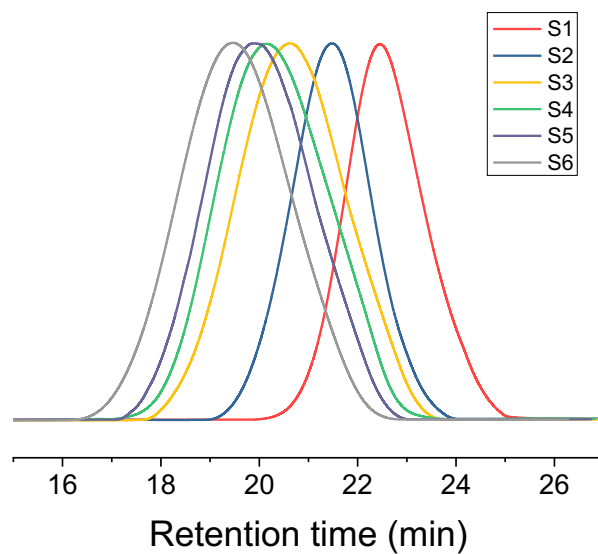
828
 829 **Supplementary Fig. 3.** ¹H NMR spectrum of P((St-PtBA)-*co*-MTL) (S2) recorded in CDCl₃ at
 830 25 °C.
 831



832

833 **Supplementary Fig. 4.** ¹H NMR spectrum of poly((St-PtBA)-co-(MI-PNIPAM)) (S3) recorded in
 834 CDCl₃ at 25 °C.

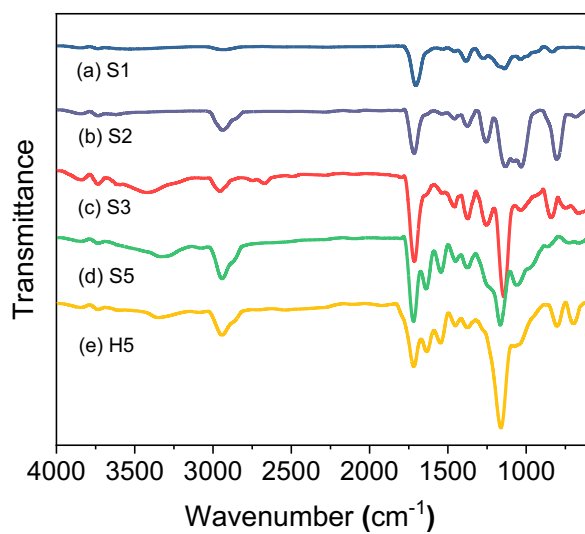
835



836

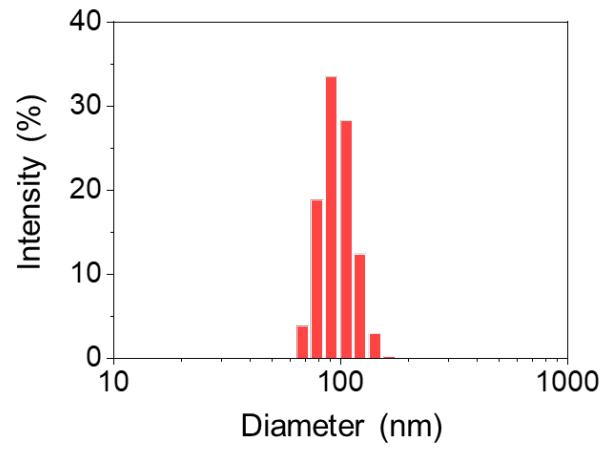
837 **Supplementary Fig. 5.** GPC traces of poly(VBHP-*co*-MTL) (S1), poly((St-*Pt*BA)-*co*-MTL) (S2),
838 poly((St-*Pt*BA)-*co*-(MI-PNIPAM)) (S3), and poly((St-*Pt*BA/PCL)-*co*-(MI-PNIPAM/PCL)) (S4-
839 S6) copolymers.

840



841
842 **Supplementary Fig. 6.** FT-IR spectra of poly(VBHP-*co*-MTL) (S1, a), poly((St-PtBA)-*co*-MTL)
843 (S2, b), poly((St-PtBA)-*co*-(MI-PNIPAM)) (S3, c), poly((St-PtBA/PCL)-*co*-(MI-PNIPAM/PCL))
844 (S5, d), and poly((St-PAA/PCL)-*co*-(MI-PNIPAM/PCL)) (H5, e).

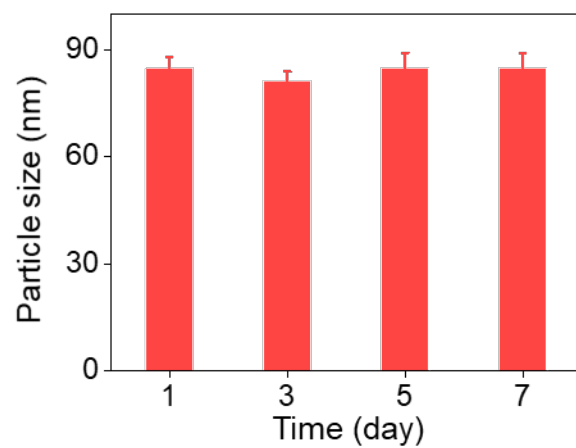
845



846

847 **Supplementary Fig. 7.** Size distribution of I/D-NAs using DLS.

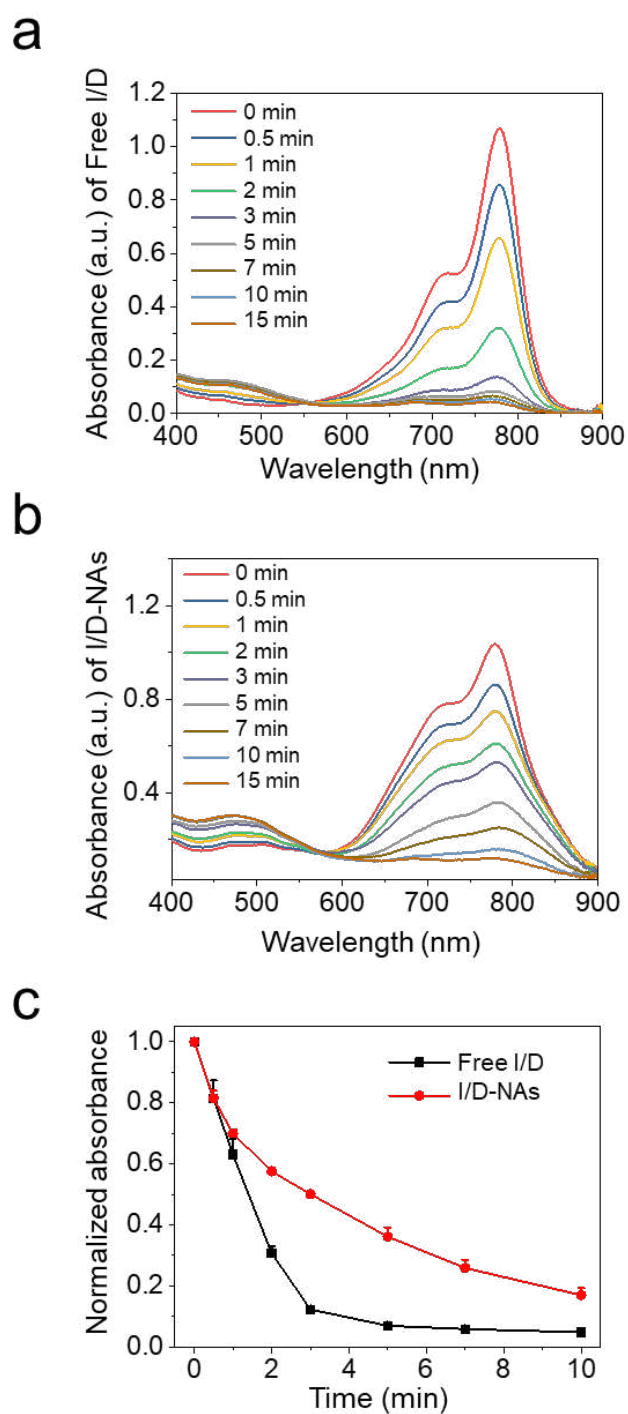
848



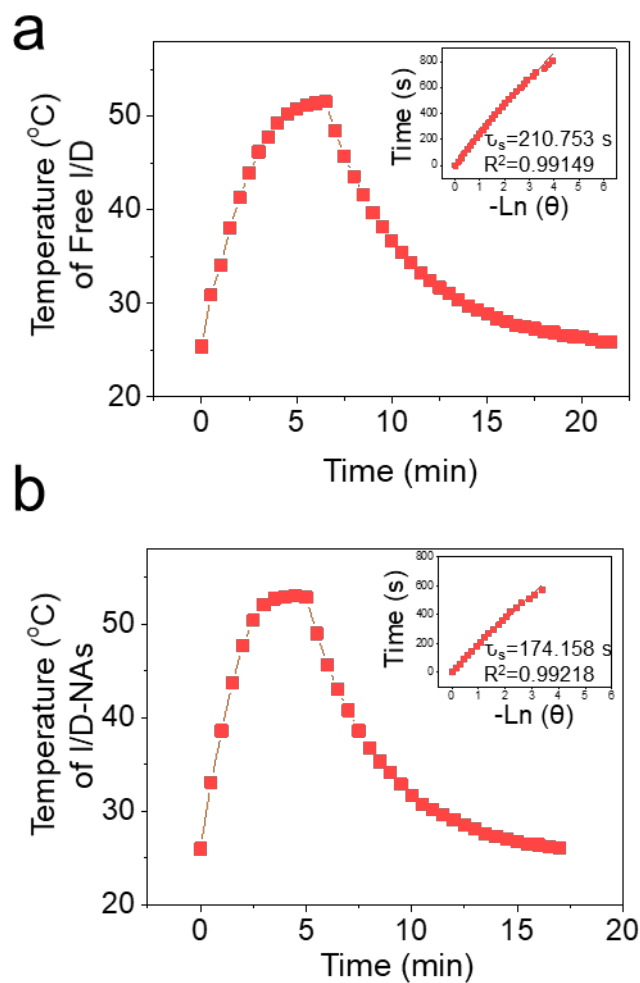
849

850 **Supplementary Fig. 8.** Particle size of I/D-NAs at 1, 3, 5 and 7 days using DLS.

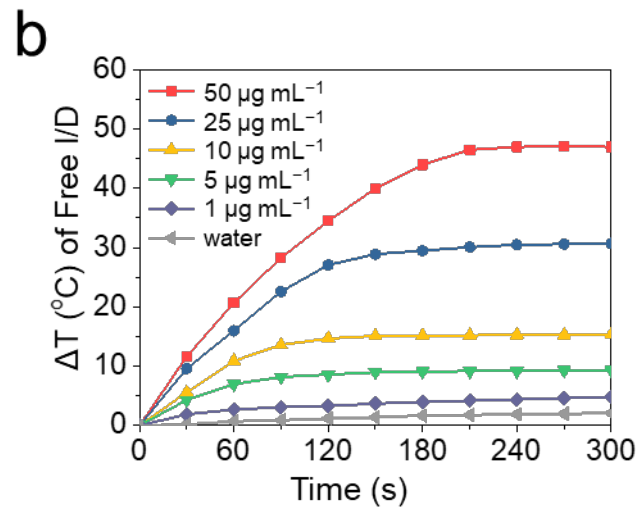
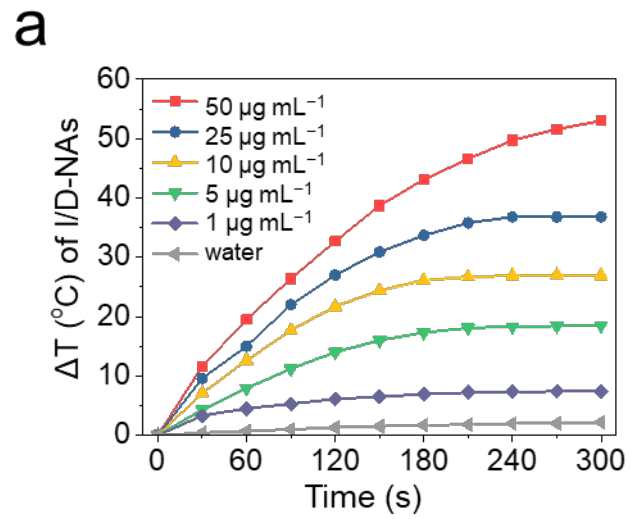
851



852
 853 **Supplementary Fig. 9.** The UV absorbance of Free I/D (a) and I/D-NAs (b) at different time after
 854 light irradiation (785 nm, 1.5 W cm⁻²). c. Normalized absorbance of Free I/D and I/D-NAs at 10.0
 855 μg mL⁻¹ ICG at different time under irradiation (785 nm, 1.5 W cm⁻²).
 856



857
 858 **Supplementary Fig. 10.** Temperature elevation of Free I/D (a) and I/D-NAs (b) with $10.0 \mu\text{g mL}^{-1}$
 859 ICG under 785 nm irradiation (1.5 W cm^{-2}), and subsequent natural cooling when removing the
 860 irradiation.
 861

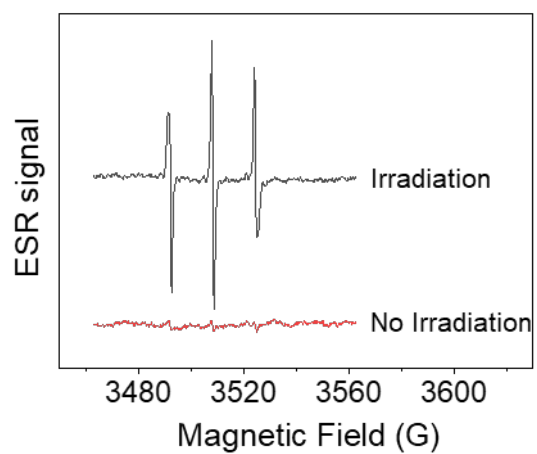


862

863 **Supplementary Fig. 11.** Temperature elevations of I/D-NAs (a) and Free I/D (b) at various

864 concentrations of ICG within 5 min irradiation (785 nm, 1.5 W cm⁻²).

865

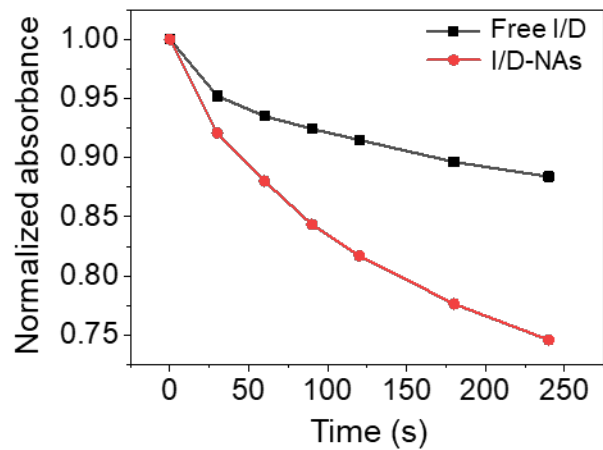


866

867 **Supplementary Fig. 12.** ESR spectra of I/D-NAs using TEMP as spin-trapping agent under 785

868 nm irradiation (1.5 W cm^{-2} , 5 min).

869

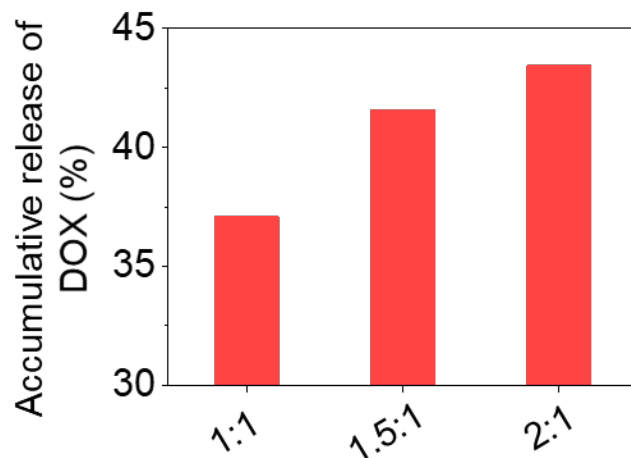


870

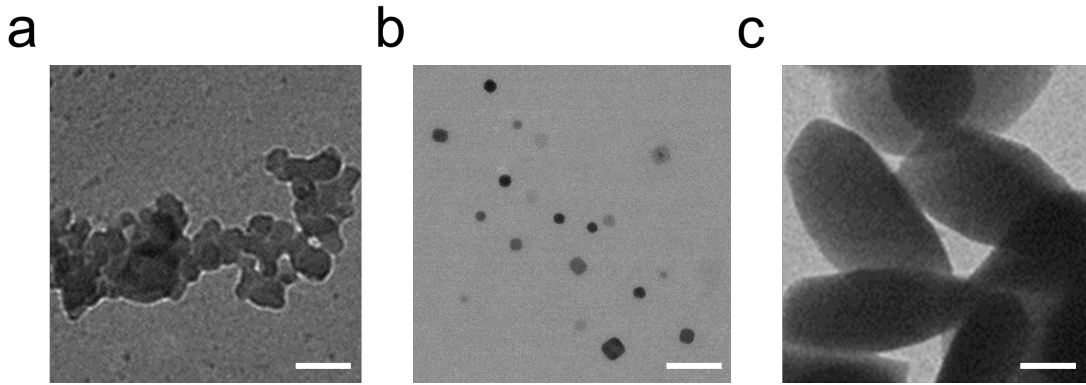
871 **Supplementary Fig. 13.** Normalized absorbances of Free I/D and I/D-NAs at various time using

872 DPBF as a probe under 785 nm irradiation at 1.5 W cm^{-2} .

873



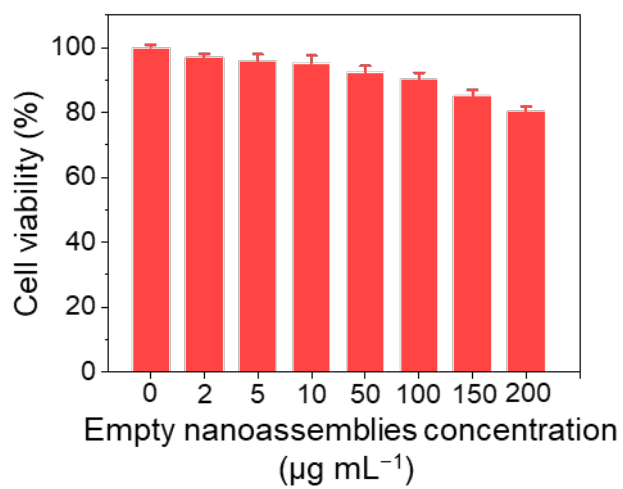
874
875 **Supplementary Fig. 14.** Accumulative releases of DOX from I/D-NAs at various ICG/DOX ratios
876 at the concentration of $80.0 \mu\text{g mL}^{-1}$ DOX in the presence of 10.0 mM DTT under 3 min light
877 irradiation during 24 h.
878



879

880 **Supplementary Fig. 15.** TEM images of I/D-NAs in various stimulative environments including
881 acidic solution of pH 5.0 (a), reduction solution with DTT after 12 h reaction time (b), and light
882 irradiation for 5 min (785 nm, 1.5 W cm⁻²) (c). (scale bar: 100 nm).

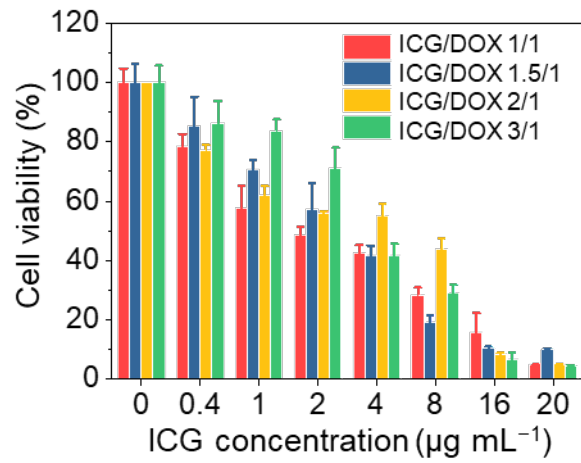
883



884

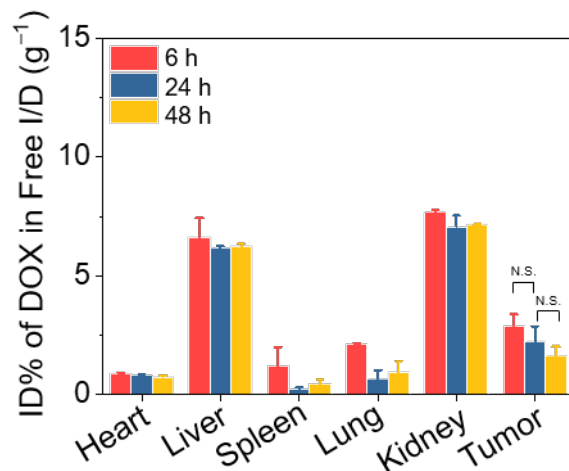
885 **Supplementary Fig. 16.** Cell viability of 4T1 cells treated with drug-free NAs.

886



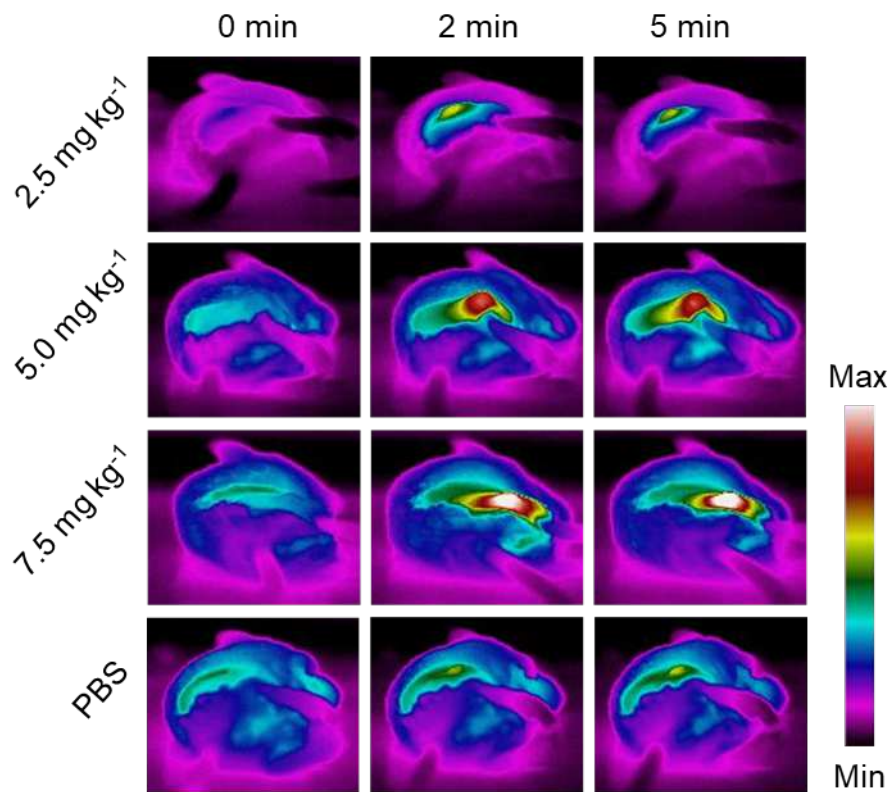
887
 888
 889
 890

Supplementary Fig. 17. Cell viability of 4T1 cells treated I/D-NAs with the ICG/DOX ratios of 3/1, 2/1, 1.5/1, and 1/1 at the different doses of ICG under 1.5 W cm^{-2} irradiation for 3 min or not.

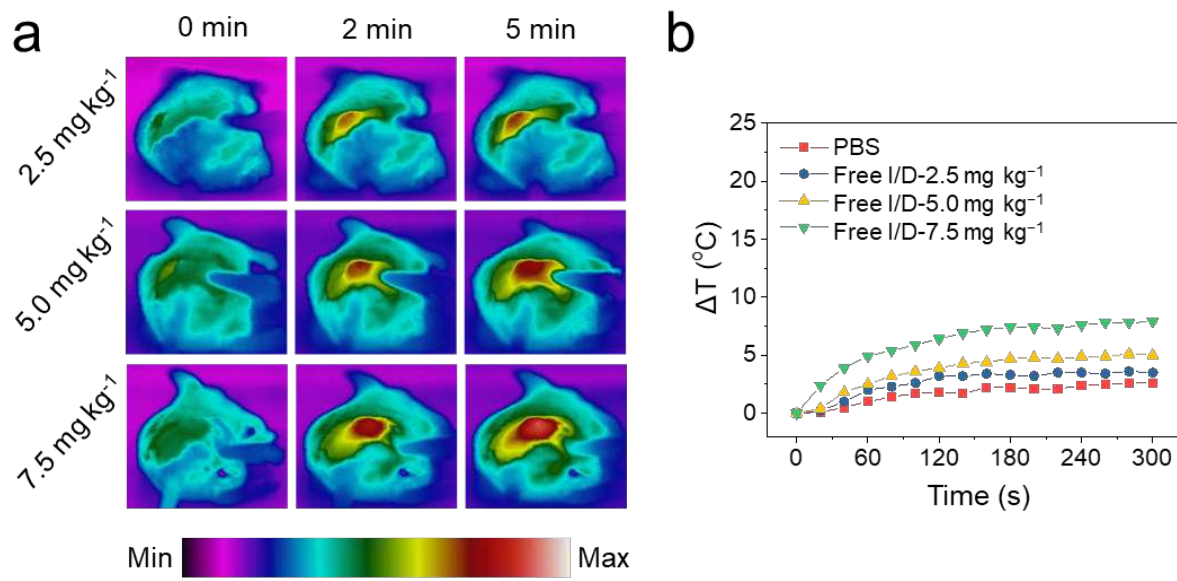


891
 892 **Supplementary Fig. 18.** *Ex vivo* distribution of DOX in heart, liver, spleen, lung, kidney, and
 893 tumour of the mice bearing 4T1 subcutaneous tumours treated with Free I/D at different time post-
 894 injection at the dose of 7.5 mg kg⁻¹ ICG. Statistical analysis was performed using two-sided
 895 student's *t*-test, $p > 0.05$.

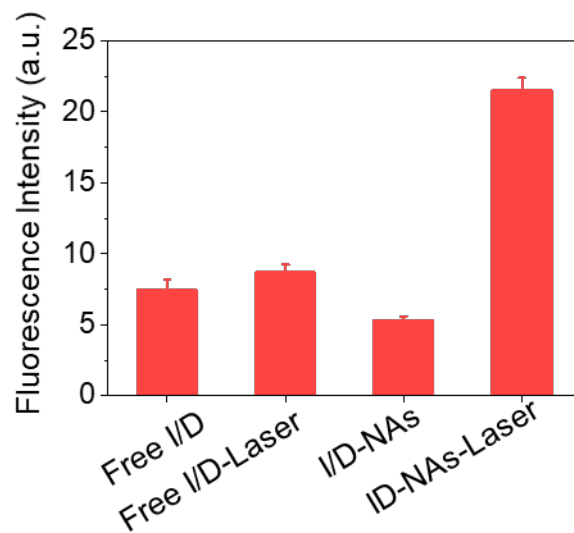
896



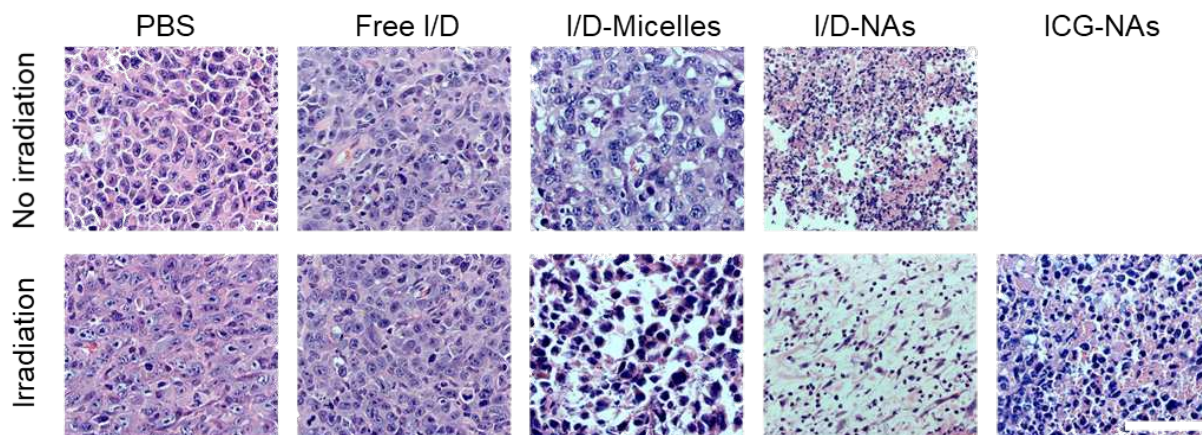
897
 898 **Supplementary Fig. 19.** Infrared thermography of the mice bearing 4T1 cells treated with I/D-
 899 NAs at different doses of ICG.
 900



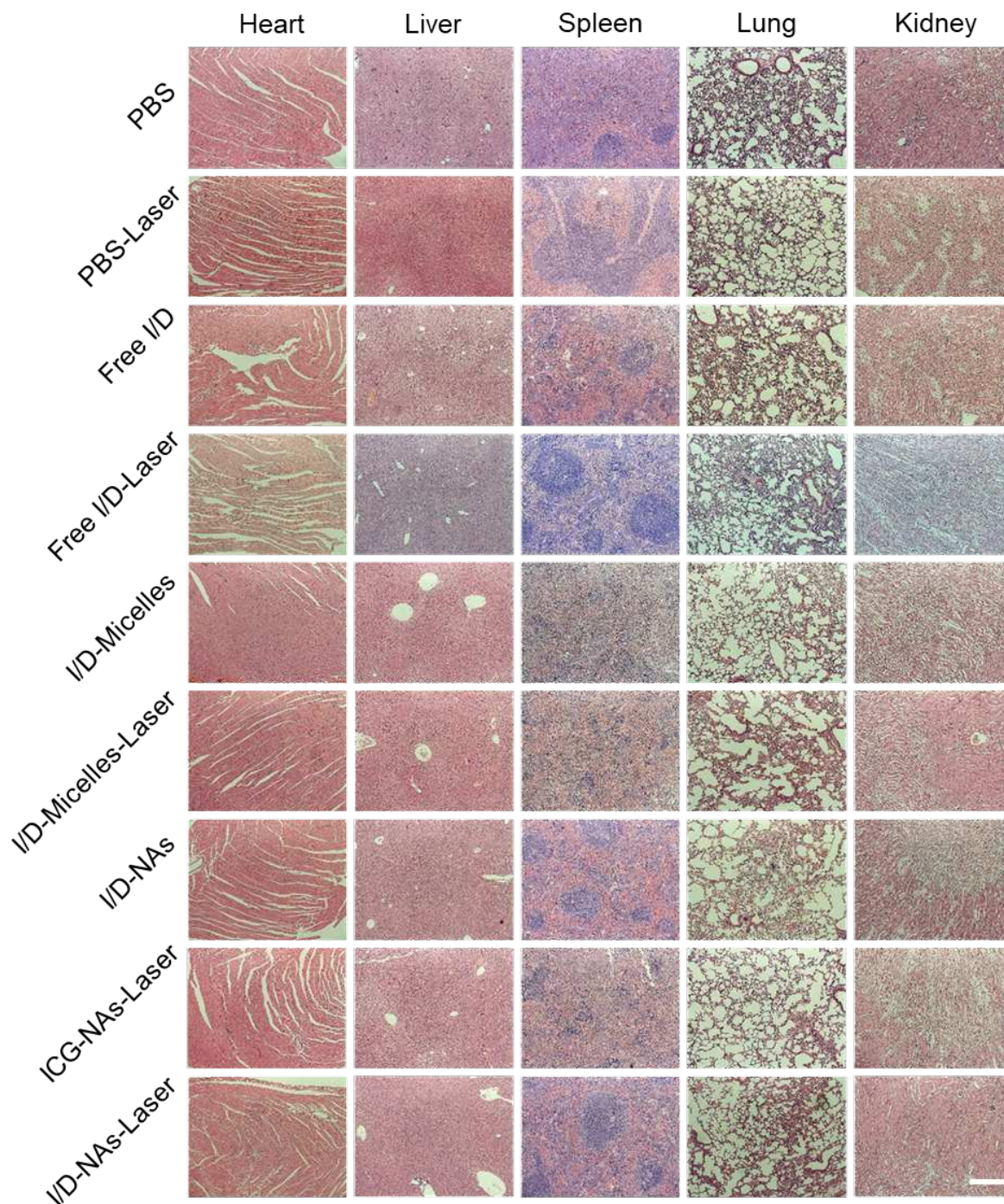
901
 902 **Supplementary Fig. 20.** Infrared thermography of the mice bearing 4T1 subcutaneous tumours
 903 treating with Free I/D at different doses of ICG (**a**) and their temperature elevations (**b**).
 904



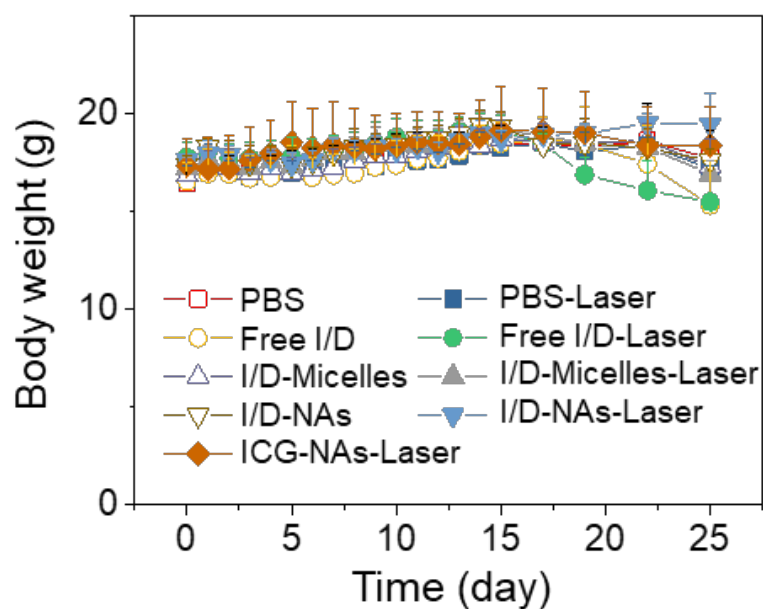
905
906 **Supplementary Fig. 21.** Fluorescence intensities calculated from DHE stained tumour sections of
907 4T1 subcutaneous tumour bearing mice treated with Free I/D and I/D-NAs at the dose of 7.5 mg
908 kg^{-1} ICG after 3 min irradiation (785 nm, 1.5 W cm^{-2}) or not.



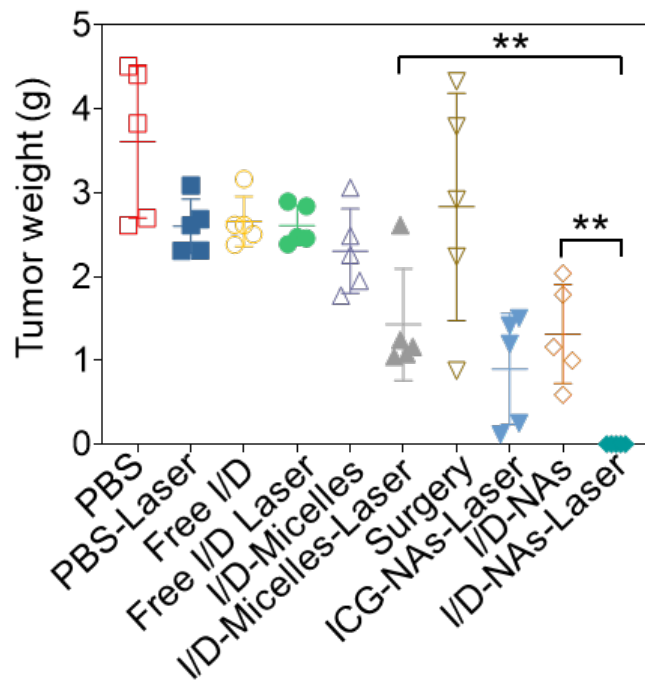
909
 910 **Supplementary Fig. 22.** Images of H&E stained tumour sections from the mice bearing
 911 subcutaneous 4T1 tumour which suffered from various formulations at the dose of 7.5 mg kg^{-1}
 912 ICG under 3 min irradiation (785 nm , 1.5 W cm^{-2}) or not at 24 h post-injection (scale bar: $50 \text{ }\mu\text{m}$).
 913



914
 915 **Supplementary Fig. 23.** Images of H&E-stained sections of heart, liver, spleen, lung, and kidney,
 916 harvested from the mice bearing 4T1 subcutaneous tumours treated with different formulations at
 917 the dose of 7.5 mg kg⁻¹ ICG (scale bar: 200 μm).
 918

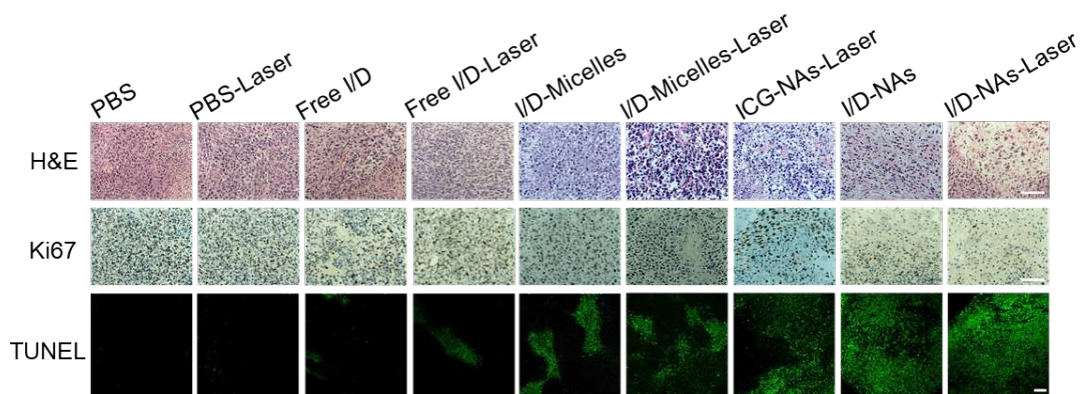


919
 920 **Supplementary Fig. 24.** Body weights of the mice bearing 4T1 subcutaneous tumours treated
 921 with Free I/D, I/D-Micelles, ID-NAs and ICG-NAs at the dose of 7.5 mg kg⁻¹ ICG with light
 922 irradiation or not during 25 days.
 923



924
 925
 926
 927
 928

Supplementary Fig. 25. Tumour weights of the mice bearing orthotopic 4T1 breast tumours treated with surgery, Free I/D, I/D-Micelles, I/D-NAs and ICG-NAs at the dose of 7.5 mg kg⁻¹ ICG under light irradiation or not at 20 days post-injection.

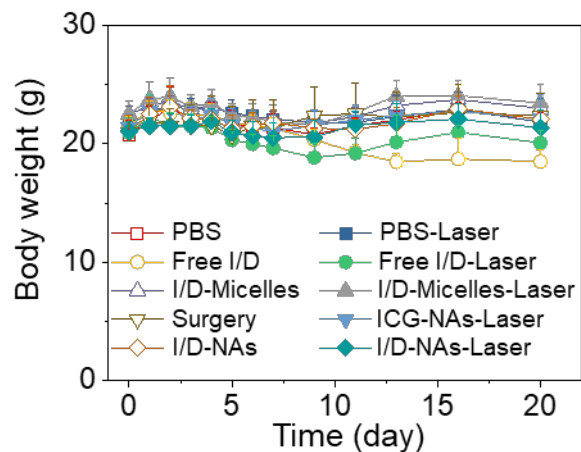


929

930 **Supplementary Fig. 26.** H&E staining images (scale bar: 50 μm), Ki67 staining images (scale bar:

931 50 μm) and TUNEL staining images (scale bar: 100 μm) of tumour sections at 6 h post-irradiation.

932



933
 934 **Supplementary Fig. 27.** Body weights of mice bearing orthotopic 4T1 breast tumours after
 935 treating with surgery, Free I/D, I/D-Micelles, I/D-NAs and ICG-NAs at the dose of 7.5 mg kg⁻¹
 936 ICG with light irradiation or not during 20 days post-irradiation.
 937

938 **Supplementary Table 1.** Results for synthesis of disulfide-functionalized copolymers including
 939 poly(VBHP-*co*-MTL) (S1), poly((St-*Pt*BA)-*co*-MTL) (S2), poly((St-*Pt*BA)-*co*-(MI-PNIPAM))
 940 (S3) and poly((St-*Pt*BA/PCL)-*co*-(MI-PNIPAM/PCL)) (S4-S6)^a

run	sample	CTA/I ^b	M	C% ^c	$M_{n,th}$ (kDa) ^d	$M_{n,GPC}$ (kDa) ^e	\mathcal{D} ^e	$M_{n,NMR}$ (kDa) ^f
1	S1	S-CPDB	VBHP/MTL	69.6	8.98	8.24	1.28	9.03
2	S2	S1	<i>t</i> BA	4.32	32.3	18.6	1.26	33.2
3	S3	S2	NIPAM	84.8	73.5	31.2	1.86	72.8
4	S4	S3	CL	75.0	109	35.6	1.90	108
5	S5	S3	CL	73.2	131	44.3	1.88	130
6	S6	S3	CL	68.9	183	59.4	1.92	185

941 ^a Reaction conditions: [VBHP]₀: [MTL]₀: [S-CPDB]₀: [AIBN]₀ = 20:20:1:0.3, [M]₀ = 1.0 mol L⁻¹,
 942 in dioxane at 70 °C for 20 h (run 1); [*t*BA]₀: [-Br]₀: [CuBr]₀: [PMDETA]₀ = 300:1:0.5:0.5, [M]₀ =
 943 3.0 mol L⁻¹, in dioxane at 60 °C for 15 h, followed by end-capping reaction to deactivate ATRP
 944 and RAFT moieties (run 2); [thiolactone]₀: [HOCH₂CH₂NH₂]₀: [NIPAM]₀: [AIBN]₀ = 1:2:30:0.01,
 945 [M]₀ = 1.0 mol L⁻¹, in DMF at 25 °C for 20 h and 65 °C for 24 h (run 3); [CL]₀: [-OH]₀: [Sn(Oct)₂]₀
 946 = *x*:1:0.2, *x* = 15 (run 4), 25 (run 5) and 50 (run 6), [M]₀ = 1.2 mol L⁻¹, in toluene at 100 °C for 20
 947 h (runs 4-6). ^b Chain transfer agent (CTA, run 1) or macroinitiator (I, other runs). ^c Monomer
 948 conversion determined by gravimetry. ^d Theoretical molar mass. ^e Apparent molar mass ($M_{n,GPC}$)
 949 and dispersity (\mathcal{D}) estimated by DMF GPC. ^f Molar mass determined by ¹H NMR analysis.

950

951 **Supplementary Table 2.** Photophysical properties of I/D-NAs and Free I/D.

Parameter	Free I/D	I/D-NAs
ROS quantum yield	0.14	0.21
Fluorescence quantum yield	0.5%	0.15%
Photothermal conversion efficiency	20.3%	24.6%

952

953 **Supplementary Table 3.** Pharmacokinetic parameters in plasma for DOX in BALB/c mice at the
954 dose of 7.5 mg kg⁻¹ ICG equivalent of Free I/D and I/D-NAs.

Parameter	Free I/D	I/D-NAs
T _{1/2α} (h)	0.1	0.1
T _{1/2β} (h)	1.2	5.2
AUC (mg·h·L ⁻¹)	20.7	60.8
CL (L·h·kg ⁻¹)	3.4	0.5

955

956 **Supplementary Table 4.** Plasma pharmacokinetic parameters of ICG from Free I/D and I/D-
957 NAs in the BALB/c mice at the dose of 7.5 mg kg⁻¹ ICG.

Parameter	Free I/D	I/D-NAs
T _{1/2α} (h)	0.1	0.1
T _{1/2β} (h)	0.8	4.9
AUC (mg·h·L ⁻¹)	10.5	90.2
CL (L·h·kg ⁻¹)	3.9	0.3

958

959 2. Supplementary Methods

960 **Materials.** The chemicals were ordered from Sigma-Aldrich unless otherwise stated. 2,2'-
961 Azobis(isobutyronitrile) (AIBN, 99%) was recrystallized twice from ethanol, ϵ -caprolactone (CL,
962 99%) was dried over CaH₂ and distilled under reduced pressure, *tert*-butyl acrylate (*t*BA, 99%,
963 Alfa-Aesar) was passed through a basic alumina column to remove the inhibitor, and *N*-
964 isopropylacrylamide (NIPAM, 97%) was recrystallized twice from the mixtures of hexane and
965 toluene. CuBr (98%) was purified by stirring in acetic acid, washing with ethanol and drying under
966 vacuum conditions. 1-Butanethiol (98%, 3a-Chemicals), dithiothreitol (DTT, 99%, Merck), tris(2-
967 dimethylaminoethyl)amine (Me₆TREN, 98%, TCI), 4-vinylbenzyl chloride (VBC, 90%, TCI),
968 *D,L*-homocysteine thiolactone hydrochloride (98%, Aladdin), *N,N'*-dimethylethylenediamine
969 (DMDA, 99%, Adamas), stannous octoate (Sn(Oct)₂, 97%), *N,N'*-dicyclohexylcarbodiimide (DCC,
970 95%, Macklin), 4-dimethylamino pyridine (DMAP, 97%, Macklin), 2-bromoisobutyric acid (98%,
971 Macklin), and other reagents with analytical grade were used as received. Anisole, acetonitrile,
972 dichloromethane, tetrahydrofuran and 1,4-dioxane were purified using standard procedures. Bis(2-
973 hydroxyethyl)disulfide di(4-(benzodithioyl)-4-cyanopentanoate) (S-CPDB)¹, 4-vinylbenzyl-3-(2-
974 bromo-2-methylpropanoyloxy)-2-hydroxymethyl-2-methylpropionate (VBHP)² and 2-
975 maleimidyl-4-thiobutylolactone (MTL)³ were synthesized according to the references.

976 977 **Synthesis of poly((St-*Pt*BA/PCL)-*co*-(MI-PNIPAM/PCL)) heterografted copolymers.**

978 Starting from a disulfide-functionalized RAFT agent S-CPDB, controlled polymerization,
979 telomerization and selective hydrolysis were combined to achieve multi-responsive heterografted
980 copolymers H4-H6 comprising two types of V-shaped side chains. The terpolymers were
981 comprised of pH-responsive poly(acrylic acid) (PAA), thermoresponsive poly(*N*-
982 isopropylacrylamide) (PNIPAM) and biodegradable poly(ϵ -caprolactone). Detailed syntheses and
983 characterizations were described below.

984 Firstly, reversible addition-fragmentation chain transfer (RAFT) copolymerization of VBHP
985 with MTL were used to synthesize poly(VBHP-*co*-MTL) (S1) containing hydroxyl, alkyl bromide
986 and thiolactone functionalities. MTL (0.493 g, 2.50 mmol), S-CPDB (84.6 mg, 0.125 mmol),
987 VBHP (0.998 g, 2.50 mmol), and AIBN (6.2 mg, 0.038 mmol) were added to a Schlenk tube,
988 followed by addition of dry 1,4-dioxane to reach a total volume of 5.0 mL. The contents were
989 degassed with bubbled nitrogen for 20 min and then subjected to polymerization at 70 °C for 20 h.

990 The polymerization solution was concentrated and repeatedly precipitated into diethyl ether, and
991 the monomer conversion was obtained as 69.6% by gravimetry. GPC analysis: $M_{n, \text{GPC}} = 8240$ Da,
992 $D = 1.28$. Based on $^1\text{H NMR}$ analysis, $\text{DP}_{\text{MTL unit}} = 4I_{4.62}/I_{7.91} = 14$, $\text{DP}_{\text{VBHP unit}} = 2I_{5.15}/I_{7.91} = 14$
993 (DP denotes number of monomer unit or degree of polymerization), and $M_{n, \text{NMR}} = 9030$ Da. ^1H
994 NMR (CDCl_3): δ 6.0-8.0 (m, PhH and ArH), 5.15 (s, ArCH₂O), 4.62 (m, CONHCH of MTL unit),
995 4.38 (s, CCH₂O of VBHP unit and COOCH₂CH₂S), 3.73 (s, CH₂OH of VBHP unit), 3.32 (m,
996 CHCHCO and CH₂S of MTL unit), 2.89 (m, OCH₂CH₂S), 0.6-2.7 (m, other CH, CH₂ and CH₃
997 from monomer units and linking group). FT-IR (ATR): 2928, 1697, 1517, 1452, 1391, 1276, 1203,
998 1161, 1104, 1047, 1008, 932, 844 cm⁻¹.

999 Secondly, poly((St-PtBA)-co-MTL) (S2) was synthesized by combination of grafting-from
1000 strategy and end-capping reaction. S1 was initially used to initiate the atom transfer radical
1001 polymerization (ATRP) of *t*BA. In a typical experiment, S1 (0.200 g, 0.310 mmol of Br), *t*BA (11.9
1002 g, 92.8 mmol), CuBr (22.3 mg, 0.155 mmol), and PMDETA (26.9 mg, 0.155 mmol) were added
1003 to a round-bottom flask, followed by addition of dry 1,4-dioxane to reach a total volume of 31 mL.
1004 The contents were degassed with bubbled nitrogen for 30 min, and then the polymerization was
1005 performed at 60 °C for 15 h. The polymerization solution was concentrated, followed by repeated
1006 precipitation into diethyl ether to isolate polymer. After vacuum drying, the resultant graft polymer
1007 with monomer conversion of 4.32% was obtained. On this basis, the alkyl bromide was deactivated
1008 by thio-bromide click reaction, and the RAFT moiety was removed by radical-induced reaction
1009 using excess AIBN. Polymer (0.664 g, 0.020 mmol), AIBN (6.6 mg, 0.40 mmol) and acetonitrile
1010 (5.0 mL) were added to a Schlenk tube under nitrogen, and the mixture was heated to 80 °C for 3
1011 h. After cooling down, triethylamine (TEA, 40.5 mg, 0.40 mmol) and butanethiol (BuSH, 36.1 mg,
1012 0.40 mmol) were added to the solution under nitrogen, followed by stirring at room temperature
1013 for 24 h. Afterwards, methyl acrylate (34.4 mg, 0.40 mmol) was injected into the solution to react
1014 with excess butanethiol. After centrifugation, the isolated solution was concentrated and
1015 precipitated into hexane to give S2. GPC analysis: $M_{n, \text{GPC}} = 18600$ Da, $D = 1.26$. Based on $^1\text{H NMR}$
1016 analysis, $\text{DP}_{\text{PtBA}} = 2I_{1.45}/(9I_{5.12}) = 13.5$, and $M_{n, \text{NMR}} = 33200$ Da. $^1\text{H NMR}$ (CDCl_3): δ 6.0-7.5 (m,
1017 ArH), 5.12 (s, ArCH₂O), 4.63 (m, CONHCH of MTL unit), 3.95-4.40 (m, COOCH₂), 3.66 (m,
1018 CH₂OH), 3.32 (m, CHCHCO and CH₂S of MTL unit), 2.88 (m, OCH₂CH₂S), 0.6-2.7 (m, other
1019 CH, CH₂ and CH₃ from polymer backbone, CH₂CH₂S of MTL unit, linking and end groups, and
1020 PtBA grafts). FT-IR (ATR): 3283, 2976, 2934, 2876, 2737, 2675, 2491, 1718, 1437, 1457, 1393,

1021 1366, 1255, 1144, 1011, 844 cm^{-1} .

1022 Thirdly, tandem amine-thiol-telemerization reactions were adopted to generate poly((St-PtBA)-
1023 *co*-(MI-PNIPAM)) (S3). In a typical run, S2 (0.332 g, 0.14 mmol of thiolactone unit) was dissolved
1024 in 2.0 mL of dry DMF with a magnetic stirring bar under nitrogen for 20 min, and then
1025 ethanolamine (17.1 mg, 0.28 mmol) was added to perform aminolysis. After stirring at room
1026 temperature for 20 h, the DMF solution (2.0 mL) containing NIPAM (0.475 g, 4.2 mmol) and
1027 AIBN (0.23 mg, 1.4 μmol) were injected into the solution under nitrogen. The reaction was
1028 conducted at 65 $^{\circ}\text{C}$ for 24 h, and S2 with monomer conversion of 84.8 % was obtained after
1029 purification. GPC analysis: $M_{n,\text{GPC}} = 31200 \text{ Da}$, $D = 1.86$. Based on $^1\text{H NMR}$ analysis, $\text{DP}_{\text{PNIPAM}}$
1030 $= I_{1.14}/(3I_{5.12}) = 25.0$, and $M_{n,\text{NMR}} = 72800 \text{ Da}$. $^1\text{H NMR}$ (CDCl_3): δ 6.0-7.5 (m, ArH and CONH of
1031 PNIPAM), 5.42 (m, NCHCO), 5.14 (m, ArCH₂O), 3.85-4.40 (m, COOCH₂ and CHNH of
1032 PNIPAM), 3.75 (m, NHCH₂CH₂OH), 3.66 (m, CCH₂OH), 3.15-3.50 (m, NHCH₂CH₂OH,
1033 CH₂CHS, and CHCHCO), 2.5-3.1 (m, CH₂S), 0.6-2.4 (m, other CH, CH₂ and CH₃ from polymer
1034 backbone, linking and end groups, and PtBA and PNIPAM grafts). FT-IR (ATR): 3277, 3075, 2973,
1035 2933, 1771, 1725, 1636, 1542, 1457, 1388, 1366, 1255, 1148, 1064, 1015, 926, 843 cm^{-1} .

1036 Fourthly, three examples of poly((St-PtBA/PCL)-*co*-(MI-PNIPAM/PCL)) (S4-S6) copolymers
1037 with different chain lengths of PCL grafts were synthesized by ring-opening polymerization (ROP)
1038 using S3 as a macroinitiator. In a typical run, S3 (0.208 g, 0.040 mmol of OH), Sn(Oct)₂ (3.2 mg,
1039 0.008 mmol), and CL (68.5 mg, 0.60 mmol) were added to a Schlenk tube under nitrogen, followed
1040 by addition of dry toluene to reach a total volume of 3.0 mL. After degassing, the contents were
1041 subjected to polymerization at 100 $^{\circ}\text{C}$ for 20 h. The product was purified by precipitation into
1042 hexane, and S4 was obtained in 75.0% of monomer conversion. GPC analysis: $M_{n,\text{GPC}} = 35600 \text{ Da}$,
1043 $D = 1.90$. Based on $^1\text{H NMR}$ analysis, $\text{DP}_{\text{PCL}} = I_{2.31}/(I_{4.48} \times \text{DP}_{\text{backbone}}) = 11$, and $M_{n,\text{NMR}} = 108 \text{ kDa}$.
1044 According to similar procedures, S5 and S6 with longer chain length of PCL segment were
1045 prepared. $^1\text{H NMR}$ (CDCl_3): δ 5.6-7.5 (m, ArH and CONH of PNIPAM), 5.10 (m, ArCH₂O), 4.48
1046 (m, OCH₂CH₂S), 3.9-4.4 (m, COOCH₂, CHNH of PNIPAM, and CH₂O of PCL), 3.1-3.8 (m,
1047 CHCHCO, terminal CH₂OH, NHCH₂CH₂O, and CH₂CHS), 0.6-3.0 (m, other CH, CH₂ and CH₃
1048 from polymer backbone, linking and end groups, and PtBA, PNIPAM and PCL grafts). FT-IR
1049 (ATR): 3285, 3074, 2970, 2935, 2869, 1724, 1644, 1543, 1458, 1389, 1366, 1243, 1151, 1104,
1050 1048, 844, 732 cm^{-1} .

1051 Lastly, three examples of amphiphilic poly((St-PAA/PCL)-*co*-(MI-PNIPAM/PCL)) (H4-H6)

1052 copolymers were generated by selective hydrolysis reaction of PtBA segments. In a typical
1053 experiment, S4 (200 mg), DCM (2.0 mL), and trifluoroacetic acid (120 mg) were successively
1054 added to a glass tube with a magnetic stirring bar, and the mixture was stirred at room temperature
1055 for 24 h. After concentration and precipitation into hexane, H4 was obtained in 98.0% of yield.
1056 Starting from S5 and S6, H5 and H6 were synthesized using similar procedures. FT-IR (ATR):
1057 3365, 2937, 2875, 1781, 1708, 1636, 1547, 1456, 1391, 1368, 1207, 1146, 805, 775, 694 cm^{-1} .

1058
1059 **Characterization.** Apparent molar mass ($M_{n,\text{GPC}}$) and dispersity (D or M_w/M_n) of various polymers
1060 were measured on a Waters 1515 gel permeation chromatography (GPC) using three MZ-Gel
1061 SDplus columns at 40 °C, where the eluent and standard samples were DMF and PMMA,
1062 respectively. ^1H NMR spectra (400 MHz) were measured on a Varian spectrometer at 25 °C using
1063 CDCl_3 . Fourier Transform Infrared (FT-IR) spectra of normal samples were measured on a Bruker
1064 Vertex 70 spectrometer. To determine the cloud point of various solutions, turbidity analysis was
1065 performed at 500 nm on a Shimadzu UV-3150 UV-vis spectrophotometer equipped with a
1066 thermoregulator.

1067

1068 **3. Supplementary References**

- 1069 1. Li, S., *et al.* Synthesis and properties of monocleavable amphiphilic comblike copolymers with
1070 alternating PEG and PCL grafts. *J. Polym. Sci., Part A: Polym. Chem.* **50**, 3135–3148 (2012).
- 1071 2. Dai, W., *et al.* Temperature and solvent isotope dependent hierarchical self-assembly of a
1072 heterografted block copolymer. *Chem. Commun.* **55**, 5709–5712 (2019).
- 1073 3. Rudolph, T., *et al.* Poly(thiolactone) homo- and copolymers from maleimide thiolactone:
1074 synthesis and functionalization. *Polym. Chem.* **6**, 4240–4251 (2015).

Figures

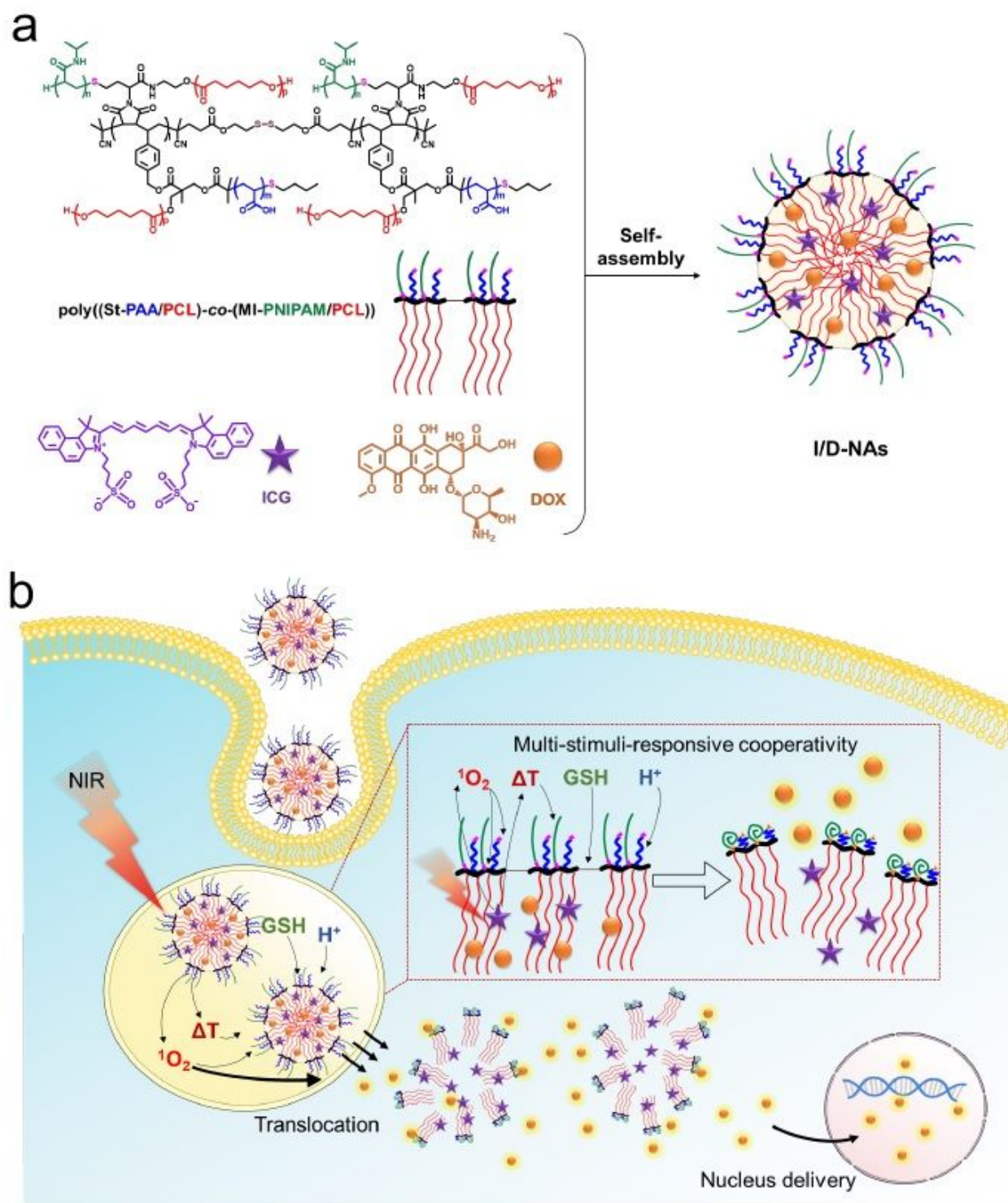


Figure 1

Schematic illustration of nanoassembly for anticancer therapy. a. Construction of H shaped miktobrush copolymer nanoassemblies with pH/reduction/temperature/ROS-responsive properties for co-encapsulating representative antitumour compounds such as indocyanine green (ICG) and doxorubicin

(DOX). b. Synergistic photo-chemotherapeutic mechanism against highly aggressive TNBC tumours through multi-stimuli-responsive drug release and ultrafast nucleus delivery.

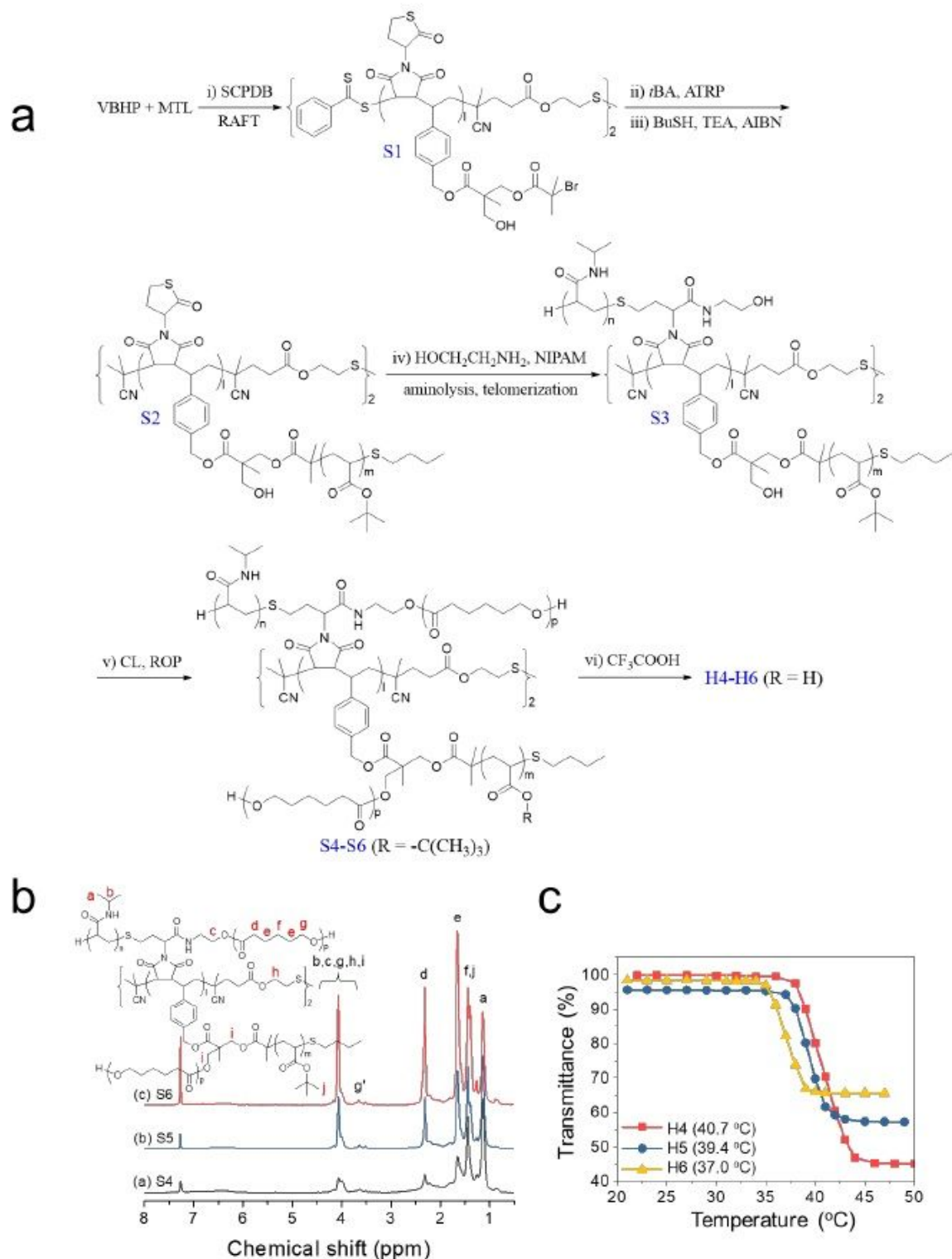


Figure 2

Synthesis and characterization of brush-like copolymers. a. Synthesis of disulfide bridged pH/reduction/temperature/ROS-responsive poly((St-PtBA/PCL)-co-(MI-PNIPAM/PCL) copolymers (H4-H6) by the combination of controlled polymerization, amine-734 thiol-telomerization and selective hydrolysis,

in which $l \approx 7$, $m \approx 14$, $n \approx 25$, and $p \approx 11$ (S4, H4), 18 (S5, H5) or 35 (S6, H6). b. ^1H NMR spectra of poly((St-PtBA/PCL)-co-(MI-PNIPAM/PCL)) copolymers recorded in CDCl_3 at 25°C , where g' denotes terminal CH_2OH of PCL grafts. c. Influence of temperature and chain length of PCL on transmittances of copolymer nanoassemblies ($\text{cp} = 1.0 \text{ mg mL}^{-1}$) formed from disulfide-bridged poly((St-PAA/PCL)-co-(MI-PNIPAM/PCL)) in aqueous solution.

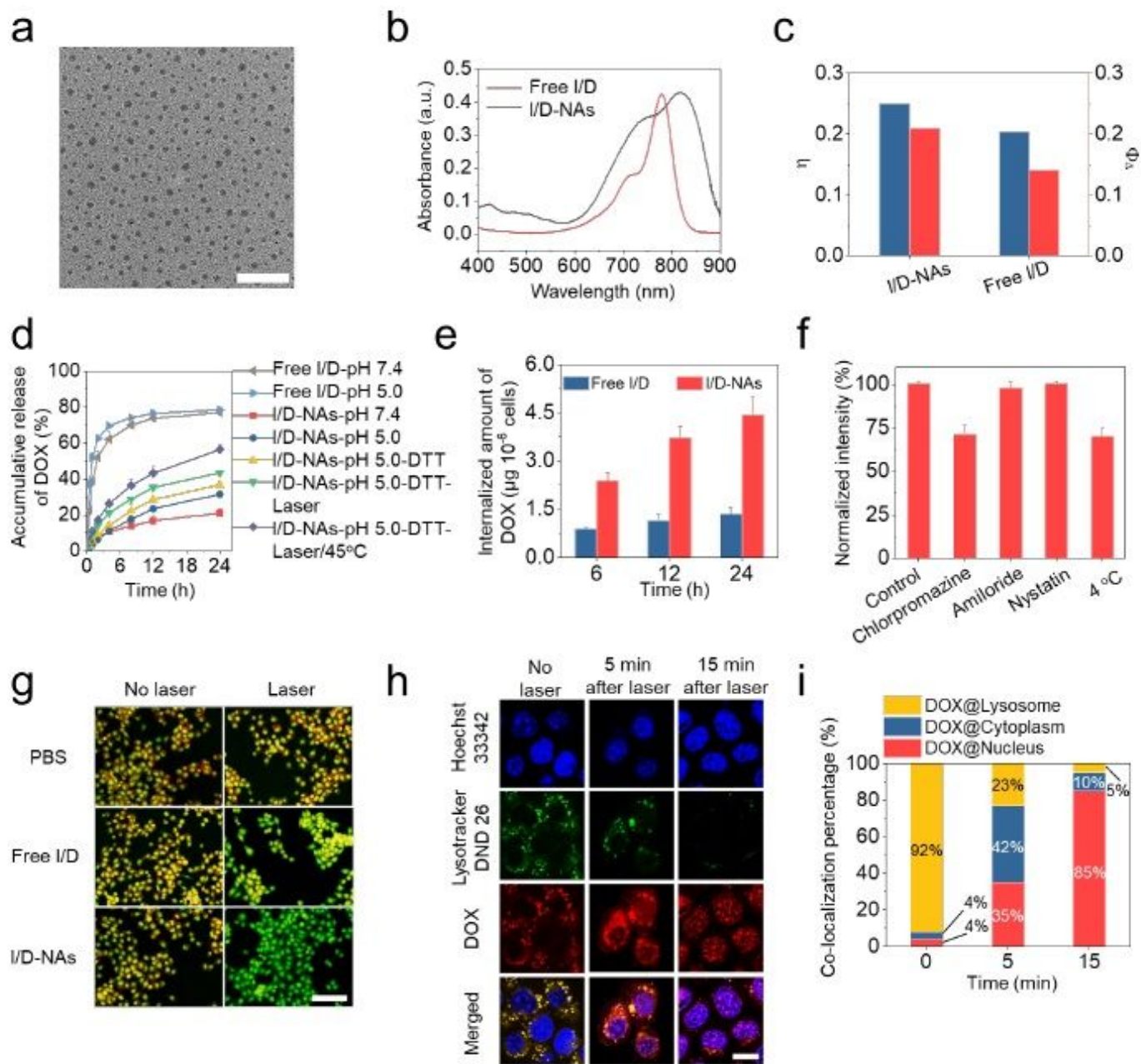


Figure 3

Enhanced lysosome-cytoplasm translocation and rapid nucleus delivery of I/D-NAs by multi-stimuli-responsive cooperativity. a. TEM image of I/D-NAs (scale bar: 500 nm). b. UV-vis absorption of Free I/D and I/D-NAs. c. Photothermal conversion efficiency (η) and Singlet oxygen quantum yield (Φ_D) of Free I/D and I/D-NAs under 785 nm laser irradiation. d. Accumulative releases of DOX from Free I/D and I/D-NAs

in various solutions. e. Internalized amounts of DOX in 4T1 cells treated by Free I/D and I/D-NAs at the dose of 10.0 $\mu\text{g mL}^{-1}$ ICG after 6, 12 and 24 h incubation. f. Cellular uptake by 4T1 cells treated with various inhibitors. g. Lysosomal disruption of 4T1 cells treated with Free I/D and I/D-NAs 750 under irradiation or not (scale bar: 20 μm). h. Confocal laser scanning microscopy images (scale bar: 20 μm) of 4T1 cells stained with LysoTracker Green DND-26 and Hoechst 33342 after 2 h incubation with I/D-NAs at the dose of 10.0 $\mu\text{g mL}^{-1}$ ICG before irradiation, as well as 5 and 15 min post-irradiation (3 min, 1.5 W cm^{-2}), respectively. i. Co-localization percentage of DOX within different organelles as indicated in h.

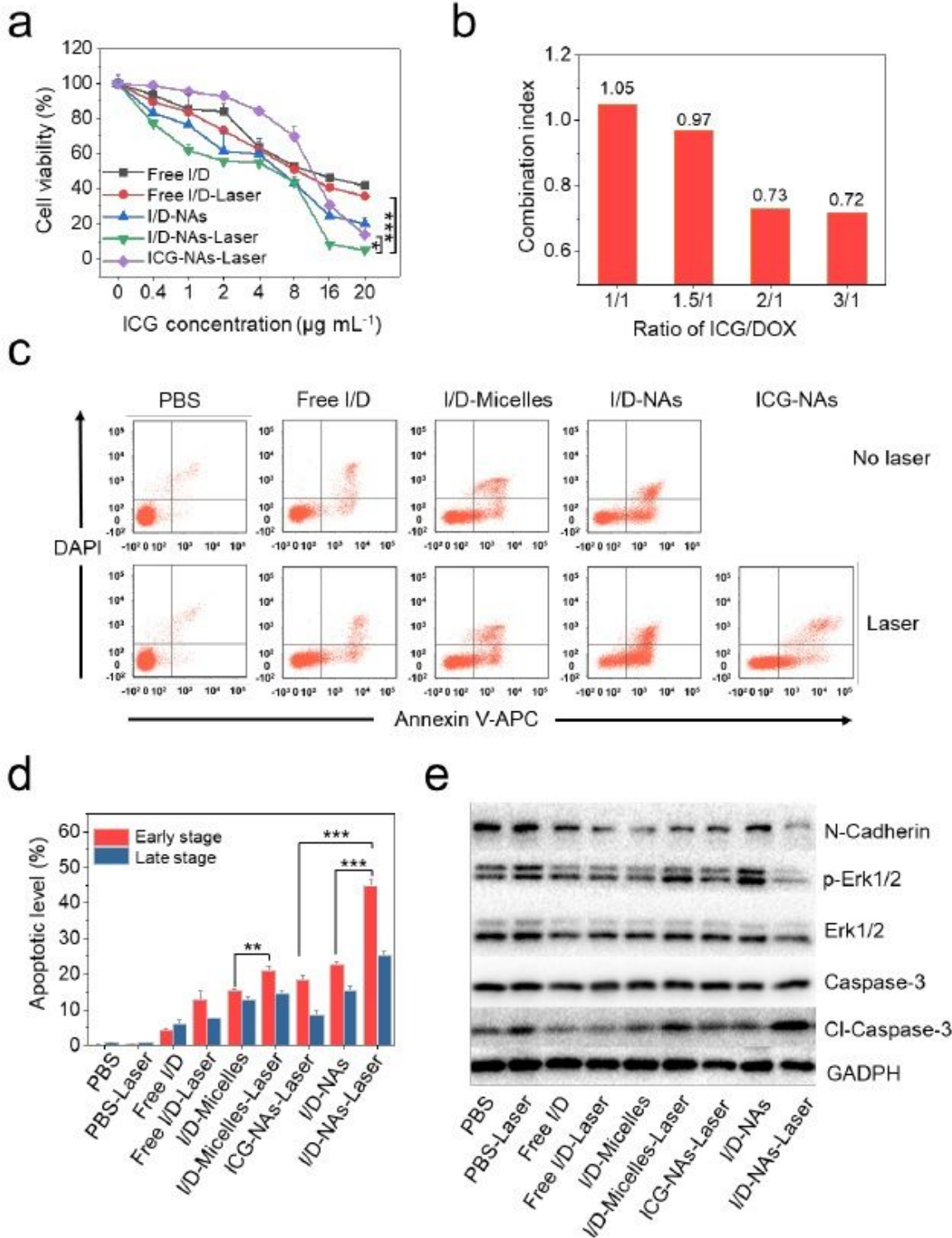


Figure 4

Cooperative cytotoxicity, antitumour and antimetastatic mechanisms of I/D-NAs. a. Cell viability of 4T1 cells treated with I/D-NAs and Free I/D under 1.5 W cm⁻² irradiation (785 nm, 3 min) or not. b. Combination index of I/D-NAs at various ratios of ICG:DOX. c. Apoptotic levels of 4T1 cells stained by Annexin V-APC/DAPI Apoptosis Detection 761 Kit after 24 h incubation with PBS, Free I/D, I/D-Micelles and I/D-NAs at the dose of 10.0 µg mL⁻¹ ICG under 3 min irradiation (785 nm, 1.5 W cm⁻²) or not and (d) their apoptotic percentages of early stage and late stage. e. Western blotting of HSP 70, N-cad, p-ERK and Cl-caspase-3 levels at 6 h post-irradiation in 4T1 cells after incubation with PBS, Free I/D, I/D-Micelles and I/D-NAs at the dose of 10.0 µg mL⁻¹ ICG under 3 min irradiation (785 nm, 1.5 W cm⁻²) or not. Statistical analysis was performed using two-sided student's t-test, *p < 0.05, **p < 0.01, and ***p < 0.001.

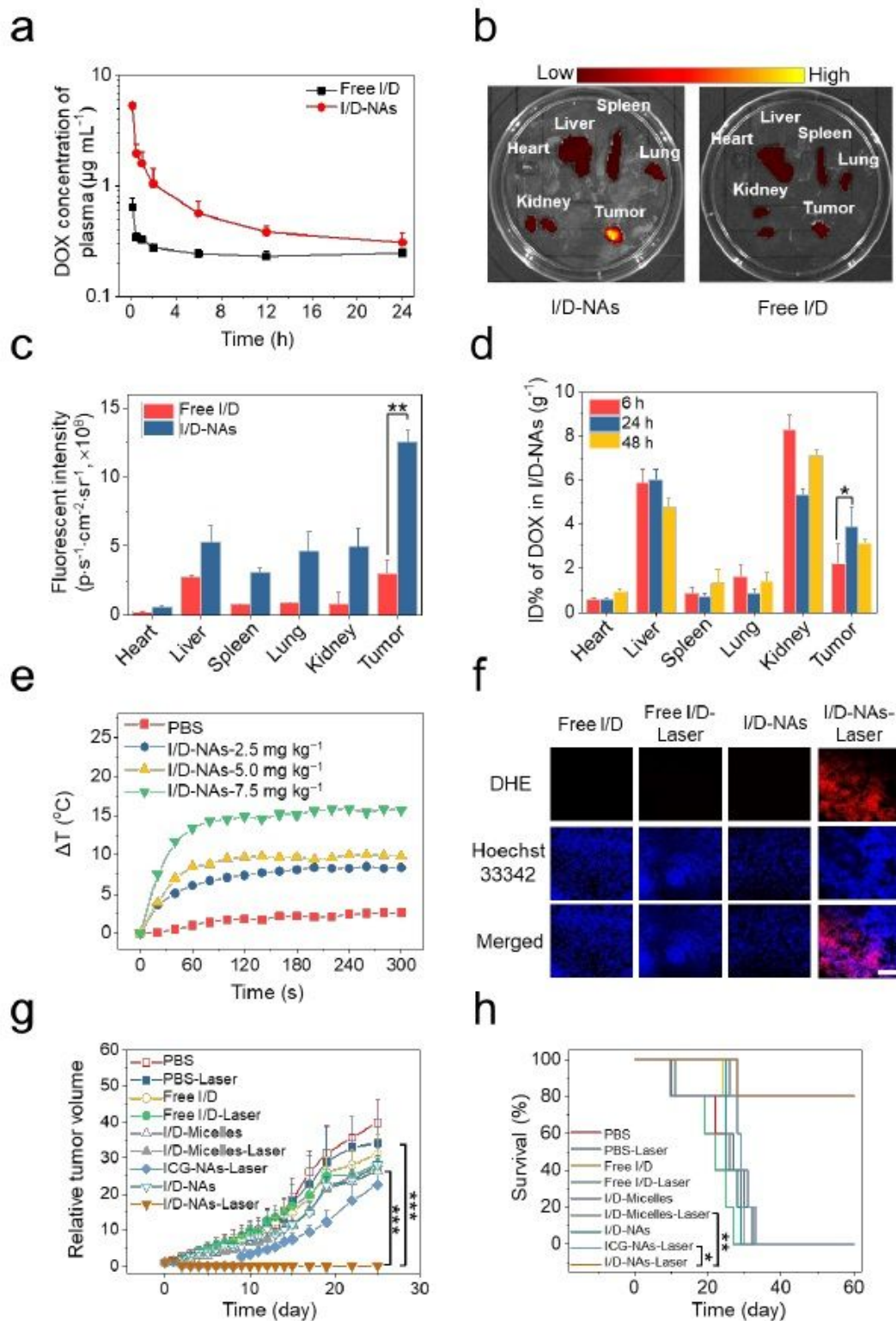


Figure 5

Photochemotherapeutic synergy of I/D-NAs against subcutaneous TNBC tumour models caused by multi-stimuli responsiveness. a. DOX concentrations in plasma from Free I/D and I/D-NAs at the dose of 7.5 mg kg⁻¹ ICG. b. Ex vivo NIRF images of heart, liver, spleen, lung, kidney, and tumour extracted from the mice bearing 4T1 cells treated with Free I/D and I/D-NAs at the dose of 7.5 mg kg⁻¹ ICG and (c) their NIRF intensities. d. Biodistribution of DOX in heart, liver, spleen, lung, kidney, and tumour of the mice

bearing 4T1 subcutaneous tumours treated with I/D-NAs at different time post-injection at the dose of 7.5 mg kg⁻¹ ICG. e. Temperature elevations of the mice bearing 4T1 cells treated with I/D-NAs at different doses of ICG under 785 nm irradiation at 1.5 W cm⁻². f. DHE staining of tumour sections treated with Free I/D and I/D-NAs at the dose of 7.5 mg kg⁻¹ ICG under 3 min irradiation or not (scale bar: 100 μm). g. Tumour growth profiles of the mice bearing 4T1 subcutaneous tumours with various treatments at the dose of 7.5 mg kg⁻¹ ICG, and (h) their Kaplan-Meier survival plots of the mice. The statistical analysis was determined by two-sided student's t-test, **p < 0.01 and ***p < 0.001. The statistical analysis was carried out using two-sided log-rank (Mantel-Cox) test for h, *p < 0.05 and **p < 0.01.

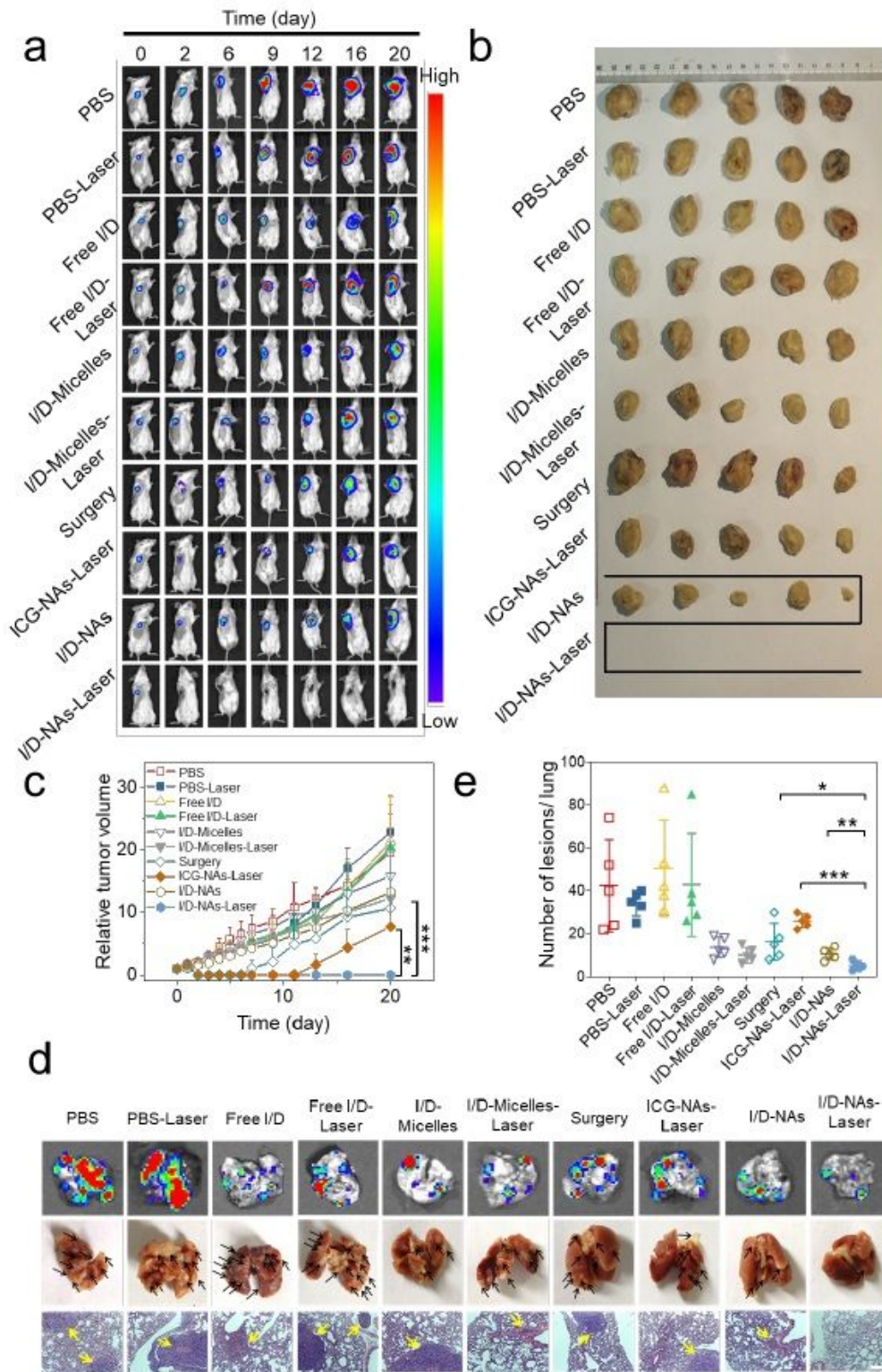


Figure 6

Photochemotherapeutic synergy of I/D-NAs against orthotopic and metastatic TNBC tumour models. a. In vivo bioluminescence images to track the tumour growth of the mice bearing orthotopic 4T1 breast tumours after various treatments. b. The photographs 790 of tumours extracted from the mice at 20 days post-injection as indicated in a. c. Tumour growth profiles of mice with various treatments as indicated in a. d. Exo vivo bioluminescence images, optical photographs and H&E staining images (scale bar: 200

μm) of the lungs from the mice at 20 days post-injection as indicated in a. e. Counts of metastatic nodules in the lungs of the mice at 20 days post-injection as indicated in a. Statistical analysis was determined by two-sided student's t-test, * $p < 0.05$, ** $p < 0.01$ and *** $p < 0.001$.